AGU PUBLICATIONS

JGR

Journal of Geophysical Research: Solid Earth

RESEARCH ARTICLE
10.1002/2016JB013194

Key Points:
- Three seismic refraction profiles constrain the crustal structure along the Kermadec arc
- The north Kermadec fore-arc hosts the Eocene Tonga arc. Back-arc crustal thickness is 4 km thinner south of the Central Kermadec Discontinuity
- Along-strike transitions in crustal structure are inherited and reflect the Cenozoic evolution of the Tonga-Kermadec margin

Supporting Information:
- Supporting Information S1

Correspondence to:
D. Bassett,
dbassett@ucsd.edu

Citation:
Bassett, D., H. Kopp, R. Sutherland, S. Henrys, A. B. Watts, C. Timm, M. Scherwath, I. Grevemeyer, and C. E. J. de Ronde (2016), Crustal structure of the Kermadec arc from MANGO seismic refraction profiles, *J. Geophys. Res. Solid Earth*, *121*, 7514–7546, doi:10.1002/2016JB013194.

Received 19 MAY 2016
Accepted 23 AUG 2016
Accepted article online 26 AUG 2016
Published online 10 OCT 2016

Crustal structure of the Kermadec arc from MANGO seismic refraction profiles

Dan Bassett[1], Heidrun Kopp[2], Rupert Sutherland[3], Stuart Henrys[4], Anthony B. Watts[5], Christian Timm[4], Martin Scherwath[2,6], Ingo Grevemeyer[2], and Cornel E. J. de Ronde[4]

[1]Scripps Institution of Oceanography, University of California, San Diego, La Jolla, California, USA, [2]GEOMAR Helmholz Center for Ocean Research, Kiel, Germany, [3]School of Geography, Environment and Earth Science, Victoria University of Wellington, Wellington, New Zealand, [4]GNS Science, Lower Hutt, New Zealand, [5]Department of Earth Sciences, University of Oxford, Oxford, UK, [6]Now at Ocean Networks Canada, University of Victoria, Victoria, British Columbia, Canada

Abstract Three active-source seismic refraction profiles are integrated with morphological and potential field data to place the first regional constraints on the structure of the Kermadec subduction zone. These observations are used to test contrasting tectonic models for an along-strike transition in margin structure previously known as the 32°S boundary. We use residual bathymetry to constrain the geometry of this boundary and propose the name Central Kermadec Discontinuity (CKD). North of the CKD, the buried Tonga Ridge occupies the fore-arc with V_P 6.5–7.3 km s^{-1} and residual free-air gravity anomalies constrain its latitudinal extent (north of 30.5°S), width (110 ± 20 km), and strike (~005° south of 25°S). South of the CKD the fore-arc is structurally homogeneous downdip with V_P 5.7–7.3 km s^{-1}. In the Havre Trough back-arc, crustal thickness south of the CKD is 8–9 km, which is up to 4 km thinner than the northern Havre Trough and at least 1 km thinner than the southern Havre Trough. We suggest that the Eocene arc did not extend along the current length of the Tonga-Kermadec trench. The Eocene arc was originally connected to the Three Kings Ridge, and the CKD was likely formed during separation and easterly translation of an Eocene arc substrate during the early Oligocene. We suggest that the first-order crustal thickness variations along the Kermadec arc were inherited from before the Neogene and reflect Mesozoic crustal structure, the Cenozoic evolution of the Tonga-Kermadec-Hikurangi margin and along-strike variations in the duration of arc volcanism.

1. Introduction

The Tonga-Kermadec subduction zone is the most linear, fastest converging [*Isacks et al.*, 1968; *Bevis et al.*, 1995], and most seismically active [*Sykes*, 1966] subduction zone with the highest density of arc-volcanic centers on Earth [*de Ronde et al.*, 2003]. In contrast to the apparent structural homogeneity of the Tonga arc [*Lonsdale*, 1986; *Austin et al.*, 1989; *W. C. Crawford et al.*, 2003; *Contreras-Reyes et al.*, 2011], marine geophysical and geochemical data have demonstrated systematic along-strike transitions in the structure of Kermadec fore-arc [*Collot and Davy*, 1998; *Davy and Collot*, 2000], back-arc [*Delteil et al.*, 2002; *Wright et al.*, 2006], and the location, character, and chemistry of the volcanic arc [*de Ronde et al.*, 2001, 2007; *Timm et al.*, 2014]. One well studied boundary occurs midway along the Kermadec margin at 32°S [*Pelletier and Dupont*, 1990] where, from north to south, the remnant Lau-Colville and active Kermadec arc ridges narrow by >50%, the back-arc and fore-arc deepen by ~1 km, and the active volcanic arc is deflected west into the deepest known back-arc basin (Figure 1). The origin and direction of causality between these coincident transitions is not clear and a relevant question considered in this study is: Do transitions in margin structure reflect; (a) the recent (<~5 Ma) mechanical behavior of the subduction interface, (b) the Cenozoic tectonic evolution of the Tonga-Kermadec subduction zone, and/or (c) the influence of variable subducting Pacific plate structure on shallow subduction mechanics, tectonics, and arc volcanism? We address this question by integrating three seismic refraction profiles with morphological and potential-field data to place the first regional constraints on crustal structure along the Kermadec arc.

Convergence between the Pacific and Australian plates began at circa 45 Ma [*Sutherland*, 1999; *Meffre et al.*, 2012] and since at least 5 Ma the plate boundary has been close to its present position along the Hikurangi-Kermadec-Tonga trench (Figure 1). Tectonic models of the intervening period are generally characterized by the eastward rollback of the Pacific plate creating a series of extensional basins, plateaus, and remnant or extinct volcanic arcs [*Kroenke and Rodda*, 1984; *Schellart et al.*, 2006; *Mortimer et al.*, 2007; *Herzer et al.*, 2011]. One prominent structure, the Tonga Ridge, is strongly expressed in the bathymetry of the Tonga fore-arc and

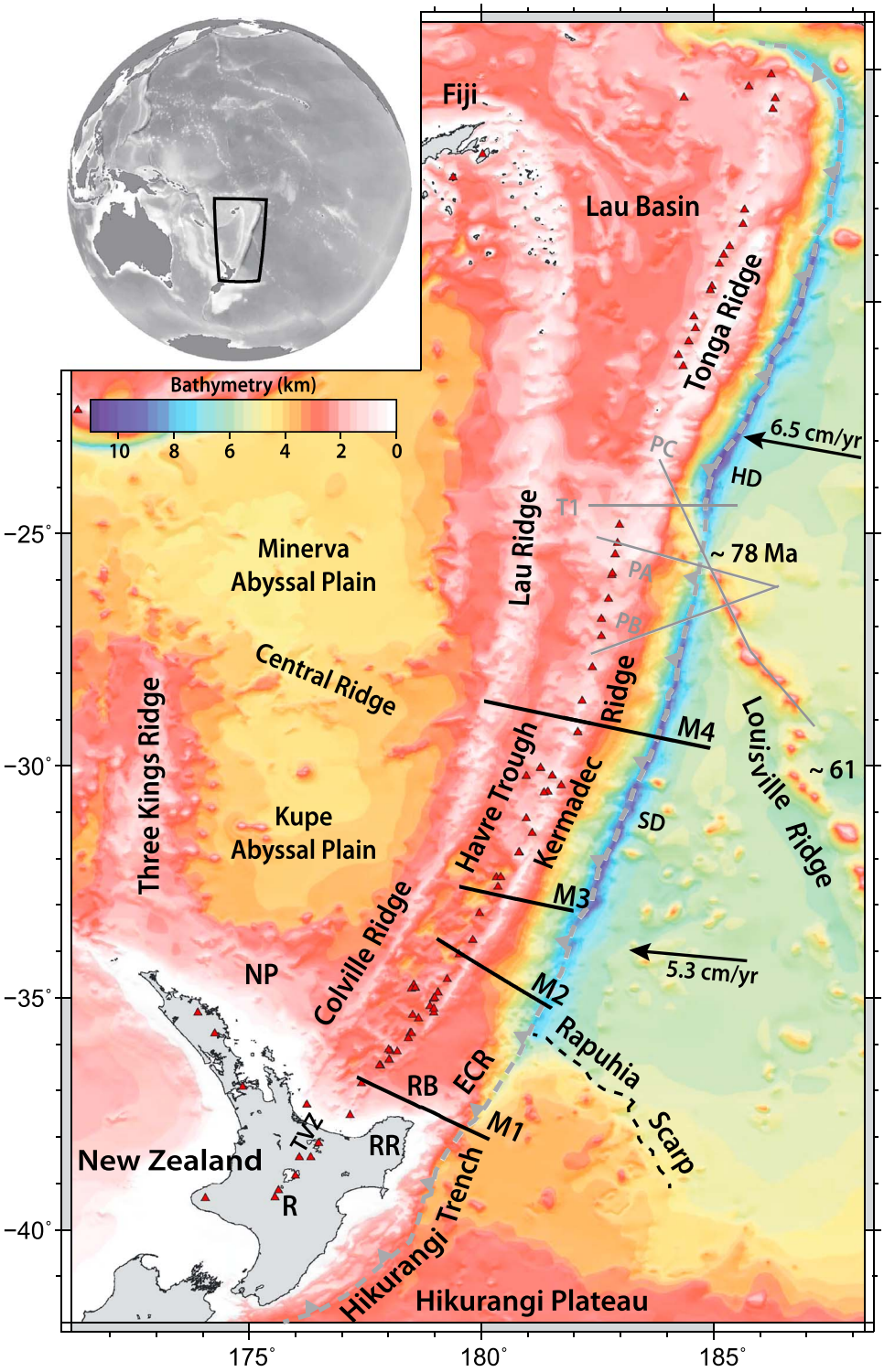

Figure 1. Bathymetric map displaying the regional tectonic setting of the Tonga-Kermadec subduction zone [*IOC et al.*, 2003]. Arrows show long-term motion of the Pacific plate relative to a fixed Australian plate [*DeMets et al.*, 2010]. Louisville Ridge seamount ages are from *Koppers et al.* [2012]. Red triangles show known locations of Holocene volcanic centers [*Wright et al.*, 1996; *de Ronde et al.*, 2001; *Simkin and Siebert*, 2002; *Wright et al.*, 2006; *de Ronde et al.*, 2007]. Lines (labeled in grey) show seismic reflection/refraction profiles with Black signifying the MANGO profiles analyzed in this study. The South Fiji Basin is west of the Lau/Colville Ridge and is structurally subdivided by a rougher and shallower Central Ridge into the Minerva and Kupe Abyssal Plains. Annotations: NP = Northland Plateau; RR = Raukumara Ranges; RB = Raukumara Basin; ECR = East Cape Ridge; TVZ = Taupo Volcanic Zone; R = Mt Ruapehu, SD = Scholl Deep; and HD = Horizon Deep.

gravity data derived during the Geosat altimeter mission suggest its buried southward extension may extend into the northern Kermadec fore-arc (Figure 1). There is no evidence for the Tonga Ridge (buried or otherwise) south of 31°S, but it is not clear whether this latitudinal extent reflects the tectonic evolution of the arc and back-arc or more recent mechanical processes influencing its preservation within the fore-arc.

Pacific plate structure clearly influences subduction dynamics along the Hikurangi margin and at the junction of the Kermadec and Tonga segments of the arc [*Collot and Davy*, 1998; *Davy and Collot*, 2000]. The early Cretaceous Hikurangi Plateau is a large igneous province (LIP) with crustal thickness of 10–23 km [*Reyners et al*., 1999; *Henrys et al*., 2006; *Davy et al*., 2008; *Scherwath et al*., 2010], and subduction of this anomalously thick crust along the Hikurangi margin has been causally related with subaerial exposure of the fore-arc along the East Coast of North Island, New Zealand [*Davy and Wood*, 1994; *Davy et al*., 2008]. Farther north near 26°S, the margin is impacted by the Louisville Ridge seamount chain. [*Timm et al*., 2013; *Bassett and Watts*, 2015a; *Stratford et al*., 2015]. Assuming the unsubducted ridge geometry is maintained, the zone of seamount subduction has been suggested to migrate south at rates up to 180 km Myr^{-1} [*Lonsdale*, 1986] and modulate a range of geological and tectonic phenomena including the rates and directions of tilting, subsidence and erosion of fore-arc crust [*Clift*, 1994; *MacLeod*, 1994; *Clift and MacLeod*, 1999], and the transition in the kinematics of back-arc extension between the Havre Trough and Lau Basin [*Ruellan et al*., 2003]. Previous interpretations have proposed that variable subducting plate structure during the Neogene is the key factor producing along-strike variations in crustal structure [*Collot and Davy*, 1998; *de Ronde et al*., 2007; *Timm et al*., 2014].

This manuscript describes the structure of the Kermadec subduction margin as constrained by three wide-angle seismic refraction profiles and the application of spectral averaging routines to regional grids and bathymetry and free-air gravity anomalies. We constrain the latitudinal extent of the Tonga Ridge, the geometry of the 32°S boundary, and place potential-field constraints on the density structure of the mantle wedge. These observations allow us to discriminate between the evolutionary models described above.

2. Geological Setting

The Hikurangi-Kermadec-Tonga subduction zone marks the boundary between the Australian and Pacific plates (Figure 1). Relative plate motion, according to the MORVEL model [*DeMets et al*., 1994, 2010], increases from highly oblique convergence at 42 mm/yr in the South Hikurangi margin to less oblique convergence at 82 mm/yr in North Tonga. Rates of back-arc rifting/spreading increase south to north from ~0 mm/yr near Mount Ruapehu at the southern tip of the Taupo Volcanic Zone (TVZ) to ~50 mm/yr in the Southern Havre Trough and ~160 mm/yr in the northern Lau Basin, contributing to the fastest subduction rates on Earth [*Karig*, 1970; *Bevis et al*., 1995].

2.1. Structure of the Fore-Arc and Subducting Pacific Plate

The northern Hikurangi margin is characterized by margin parallel transitions in crustal structure in both the Australian fore-arc and subducting Pacific plates (Figure 1). In the fore-arc, the anomalously high topography of the Raukumara Ranges (RR) [*Walcott*, 1987] transforms northeast along strike into the deep ($<$10 km sediment thickness, $>$2 km water depth) Raukumara Basin (RB) [*Sutherland et al*., 2009]. Moho depth beneath the western Raukumara Peninsula is $>$25 km [*Reyners et al*., 1999]. By contrast, the Raukumara Basin is floored by 5–8 km thick crust and the fore-arc Moho shallows from ~17 km within the central basin to $<$12.5 km within the Havre Trough, $<$15 km within the northern Raukumara Plain and 10–15 km near the East Cape Ridge [*Bassett et al*., 2010].

The structure and seismic stratigraphy of the Raukumara Basin is described and correlated with onshore geology by *Sutherland et al*. [2009]. The basin contains one of the thickest (i.e., 5–8 km) sequences of Late Cretaceous and Paleogene passive margin sediments in New Zealand (Megasequence X), a ~10,000 km^3 submarine landslide emplaced west or northwestward (Megasequence Y) and a Neogene subduction margin megasequence (Megasequence Z). *Sutherland et al*. [2009] interpret the basin stratigraphy as an east verging thrust wedge and suggest that the western part of Raukumara basin preserves the Cretaceous Gondwana trench slope. Paleomagnetic declination anomalies show that the Raukumara Peninsula has rotated with the Australian plate since 22–19 Ma [*Roberts*, 1992; *Rowan and Roberts*, 2005, 2008].

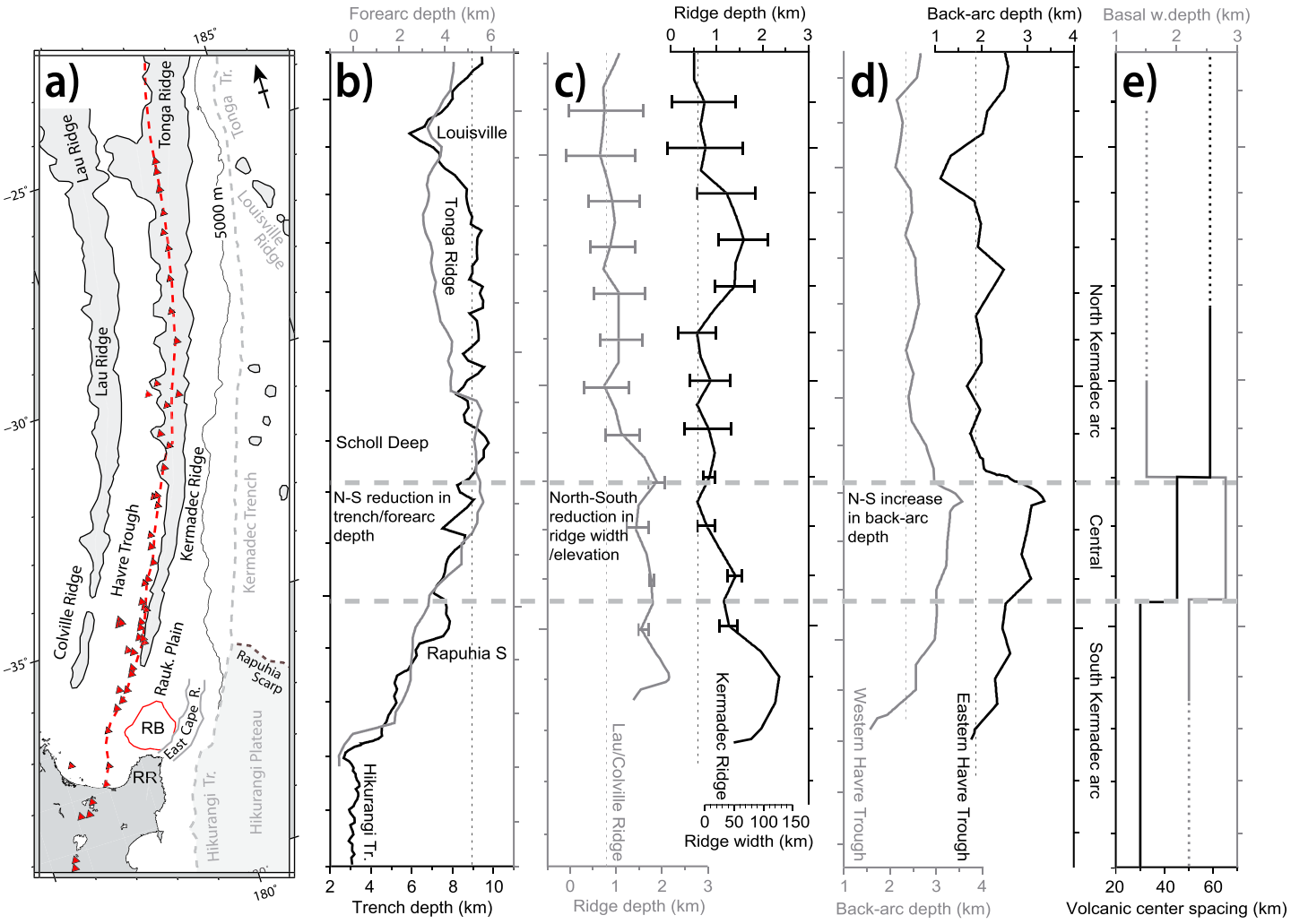

Figure 2. Along-strike variations in margin structure. (a) Map showing the simplified physiography of the Kermadec margin. Red triangles and dashed line show arc volcanoes and the arc front respectively. Solid red line outlines Raukumara Basin (RB). RR = Raukumara Ranges and East Cape R = East Cape Ridge. (b) Water depth along the trench (Black) and fore-arc trench-slope equidistant between the trench and arc (Grey). (c) Water depth along the Lau/Colville (grey) and Kermadec (black) ridges. Horizontal bars show ridge width. (d) Water depth in the Havre Trough back-arc basin. (e) Mean spacing (black) [*de Ronde et al.*, 2007] and basal water depths (grey) [*Wright et al.*, 2006] of arc volcanic centers.

On the subducting Pacific plate, the Rapuhia Scarp (Figure 1) marks the northern boundary of the Hikurangi Plateau LIP and a transition to Mesozoic oceanic crust [*Davy and Wood*, 1994; *Davy et al.*, 2008]. Immediately north of this scarp, the Kermadec trench deepens from <6.0 to >8.0 km and the trench slope break migrates 20–35 km nearer the Kermadec Ridge (Figures 2a and 2b) [*Davy and Collot*, 2000]. The shallow near-trench gradient (~1.5°), greater fore-arc water depth between 35°S and 32°S, and a ~40 km wide lower slope terrace extending to ~31°S have all been linked to tectonic erosion associated with Hikurangi plateau subduction [*Davy and Collot*, 2000]. The Kermadec trench is deepest near 32°S and reaches ~10 km at Scholl Deep (Figure 2b).

Between 31°S and 25°S, the trench is ~9 km deep, the fore-arc is ~150 km wide and has a mean trench-slope gradient of ~7° within 35 km of the trench-axis and <2° east of the Kermadec Ridge. Regional gravity grids derived from satellite altimetry [*Sandwell and Smith*, 2009] show the Tonga Ridge occupying the inner fore-arc. The gravity anomaly associated with the Tonga Ridge has not been recognized south of ~31°S and the increase in fore-arc water depth near this latitude is interpreted by *Collot and Davy* [1998] as marking the northern boundary of tectonic erosion associated with Hikurangi Plateau subduction (Figure 2b).

The Louisville Ridge collision zone (27°S–24.5°S) is characterized by a 3 km reduction in trench depth, a 15° anticlockwise rotation of the trench-axis, a 20% reduction in the width of extensional bend faulting in the

subducting Pacific plate and a rough, hummocky fore-arc on the overthrusting Australian plate [*Bassett and Watts*, 2015a; *Stratford et al*., 2015]. 250 kilometers north of the contemporary collision zone, Horizon Deep (water depth ~10.8 km) has been associated with tectonic erosion and extensional collapse of the fore-arc in the wake of seamount subduction (Figure 1) [*Lonsdale*, 1986; *Ballance et al*., 1989].

In contrast to the segmented character of the Kermadec fore-arc, the Tonga fore-arc appears from available data to be largely homogeneous along strike and is occupied by the Tonga Ridge at least as far north as 18.5°S (Figure 1) [*Lonsdale*, 1986; *Austin et al*., 1989; *W. C. Crawford et al*., 2003; *Contreras-Reyes et al*., 2011].

2.2. Structure and Character of the Kermadec Arc and Back-Arc

Along the Kermadec margin, systematic changes in the location, character, and chemistry of the volcanic arc have been recognized and correlated with coincident changes in margin structure [*Wright*, 1997; *Ballance et al*., 1999; *Wright et al*., 2006; *Timm et al*., 2013, 2014]. South of 35°S and west of the Raukumara Basin, the Havre Trough is ~150 km wide. Average water depth is between 2 and 2.5 km but locally exceeds 3 km in the Ngatoro Rifts (Figure 2d). The bounding Kermadec and Colville Ridges are generally weakly expressed, $\leq$30 km wide with elevations $<$1 km relative to the Havre Trough (Figures 2c and 2d). Swath mapping has revealed at least 13 volcanic edifices, which have a mean spacing of 30 km and include basaltic-andesitic stratovolcanoes and silicic calderas with basal water depths typically $\leq$2.5 km (Figure 2e) [*Gamble and Wright*, 1995; *Wright and Gamble*, 1999; *de Ronde et al*., 2007].

Between ~32°S and 34°S, the Colville and Kermadec Ridges remain narrow (width $<$40 km) but increase in mean elevation to 1.5–2.0 km above the Havre Trough. This is the deepest segment of the Havre Trough (Figure 2d). Mean water depth is $>$3.0 km and locally exceeds 3.7 km in sediment starved rift basins [*Delteil et al*., 2002]. Back-arc extension is distributed across the Havre Trough, but shallow seismicity [*Pelletier and Louat*, 1989] and volcanism [*Wright*, 1994] suggest that recent tectonism is focused near the contemporary volcanic arc. Rift fabric is oblique (~20° clockwise) to the back-arc basin axis [*Wright et al*., 1996; *Delteil et al*., 2002]. Arc volcanic centers have a mean spacing of 45 km, basement elevations $>$3.0 km below sea level (Figure 2e), and are predominately stratovolcanic cones of low-K series basalt and basaltic andesite [*Wright et al*., 2006; *de Ronde et al*., 2007].

At 32°S the arc front is offset 15–25 km toward the trench, coincident with a $>$1 km shoaling in the mean back-arc water depth and a factor of ~2 increase in the width of remnant and active arc ridges (Figure 2) [*Pelletier and Dupont*, 1990; *Collot and Davy*, 1998; *Wright et al*., 2006; *de Ronde et al*., 2007; *Wysoczanski et al*., 2010]. North of 32°S, the Kermadec Ridge is at least 1 km high (relative to the back-arc) and 60 km wide. The Lau Ridge is $>$1.5 km high and $>$75 km wide (Figure 2c). The Havre Trough is shallow (~2.5 km) and variably sedimented within perched and rifted subbasins in the west and composed of rugged, high standing (~2 km), and sediment starved volcanic basement in the east [*Delteil et al*., 2002]. Between 29°S and 32°S, merging of the active arc front with the Kermadec Ridge increases the predominance of caldera volcanoes with the mean spacing of volcanic centers extending to 58 km [*de Ronde et al*., 2003].

Silicic and bimodal volcanism is restricted to arc segments where basal water depths are shallower than 2.7 km and typically 1.5–2.5 km (Figure 2e) [*Wright et al*., 2006]. Predominantly basalt and basaltic andesite has been recovered from the deeper central Kermadec arc, where volcanic edifices have basal water depths $\geq$3.0 km. Mean constructional volumes for deeper ($\geq$3.0 km; $n = 7$) volcanic edifices are 140 km^3, which is a factor $>$2 larger than the mean constructional volume (55 km^3) for edifices with shallower basal water depths [*Wright et al*., 2006]. *de Ronde et al*. [2007] demonstrate systematic variations in the mean spacing of volcanic centers between the southern, central, and northern segments of the Kermadec arc (Figure 2e). They also show that the intensity of hydrothermal activity is more subdued in the deeper central segment of the Havre Trough.

3. Data

3.1. Active-Source Seismic Profiles

This manuscript is focused on wide-angle seismic profiles acquired across the Kermadec arc on board the R/V *SONNE* as part of the MANGO (Marine Geoscientific Investigations on the Input and Output of the Kermadec subduction zone) project [*Flueh and Kopp*, 2007]. The southernmost profile (M1) is presented in *Scherwath*

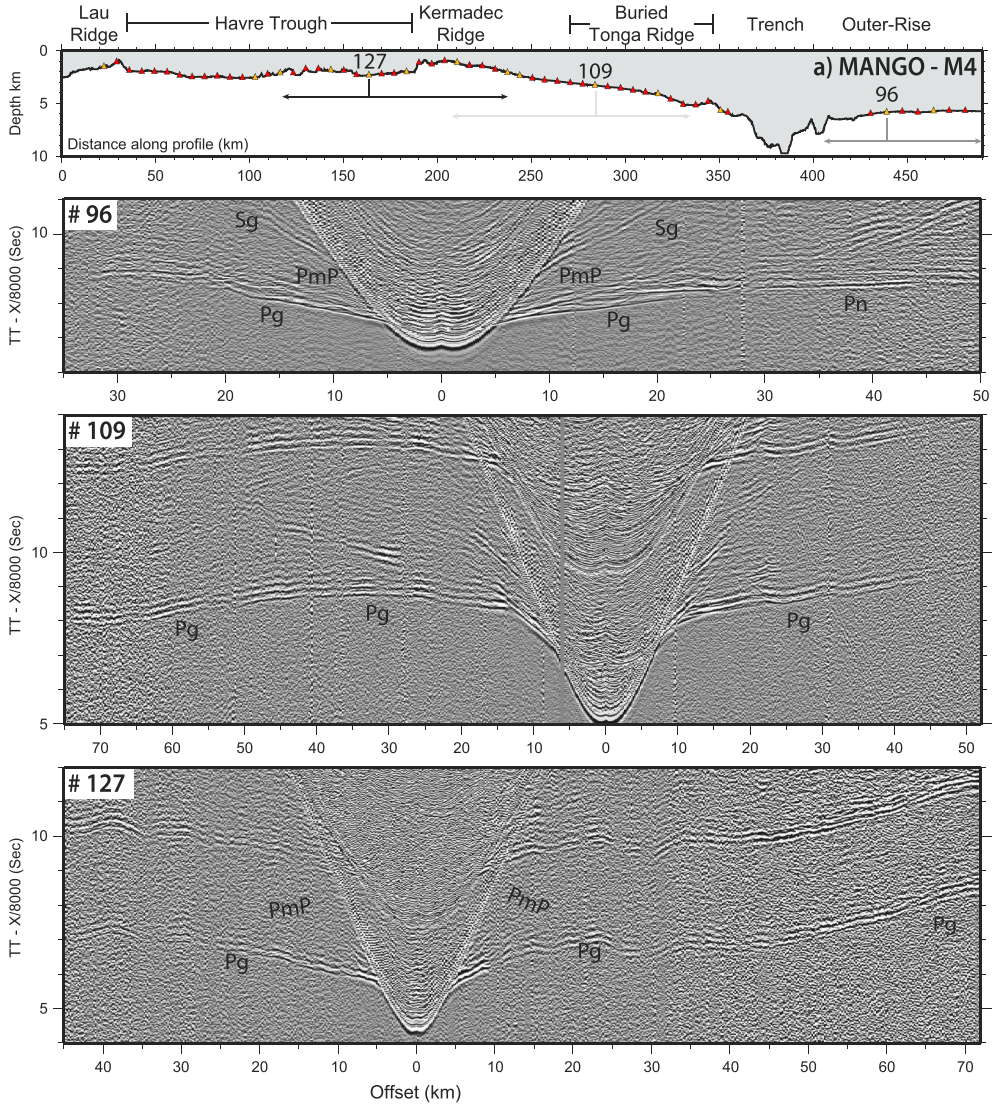

Figure 3. Wide-angle seismic data along profiles (a) MANGO 4 (M4), (b) MANGO 3 (M3), and (c) MANGO 2 (M2). Top panel shows water depth, station locations (triangles), and the distribution of shots shown in the receiver gathers below. Bottom panels show examples of wide-angle seismic data and interpreted phases. Record sections, interpretations, and associated raypaths for OBS/H marked by yellow triangles are shown in the supporting information.

et al. [2010], and this manuscript presents results from the three profiles (M2, M3 and M4) farther north (Figure 1). Profiles M1–M4 are joint Multi Channel Seismic (MCS) reflection and wide-angle seismic refraction profiles acquired in March 2007 (SO192-1). MCS data were acquired using a short (<200 m) 16 channel streamer provided by GNS Science. Wide-angle data were recorded by GEOMAR Ocean Bottom Seismographs/Hydrophones (OBS/H) spaced 6–7 km apart. The seismic source comprised eight Sercel G-Guns arranged in two four-gun subarrays with a combined volume of 64 L and fired at 3000 psi with a 60 s (~150 m at 4.5 knots) shot interval.

Wide-angle data were processed using gated Wiener deconvolution (gate 3 s, overlap 1 s, operator length, 1 s) and frequency filtering (ramp frequencies 2–5 and15–30 Hz). The collective data set comprised 116 receiver gathers resulting in >235,000 travel time interpretations. The degree of precision in interpreted arrivals ranges from 50 ms to 250 ms depending on noise levels and relationships to overlapping arrivals. The vast majority of arrivals have a precision of <100 ms. Examples of wide-angle data acquired along each profile are presented in Figure 3. Additional examples of receiver gathers interpreted arrivals and

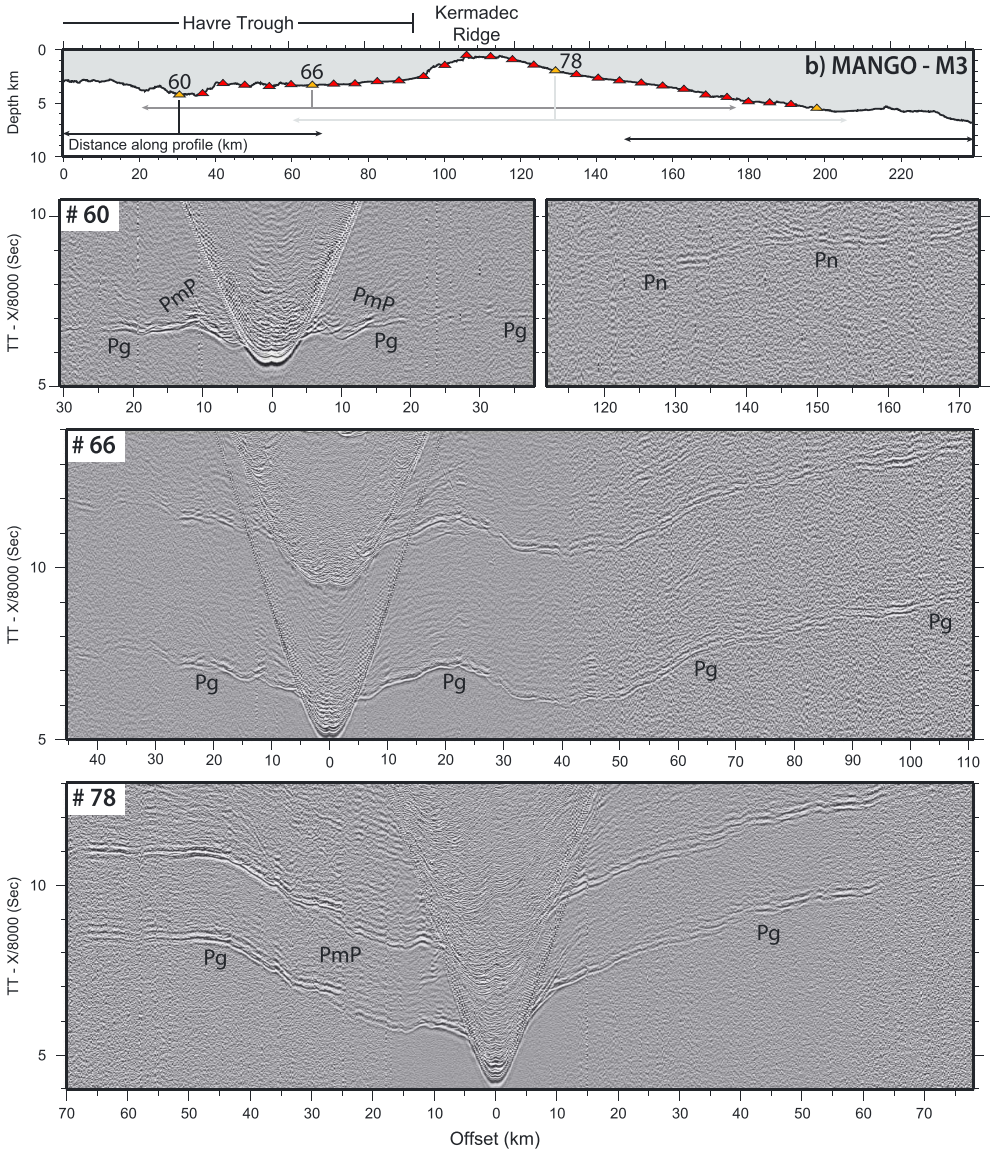

Figure 3. (continued) b) Wide-angle seismic data along profile MANGO 3 (M3).

associated raypaths for OBS/H marked by yellow triangles are shown in the supporting information Figures S3, S6, and S9.

4. Forward Velocity Modeling

4.1. Model Construction

Forward layered *P* wave velocity (V_P) models were constructed using the ray tracing and travel-time inversion method of *Zelt and Smith* [1992]. We adopted the same forward modeling methodology applied in the Louisville collision zone [*Stratford et al.*, 2015] and southern Kermadec arc [*Scherwath et al.*, 2010] to allow direct comparison of crustal sections along strike.

Layered seismic velocity models are constructed by linearly interpolating vertically and horizontally between V_P nodes positioned on layer boundaries. The water layer is defined from swath bathymetric data and by the travel times of the direct arrival and seafloor multiple. Wide-angle refracted arrivals with offsets of ≤30 km are used to define shallow fore-arc V_P structure. Refracted arrivals at greater offsets turning within the crust (P_g) and mantle (P_n), and wide-angle reflections from the Moho (P_mP) then constrain the deeper structure of the

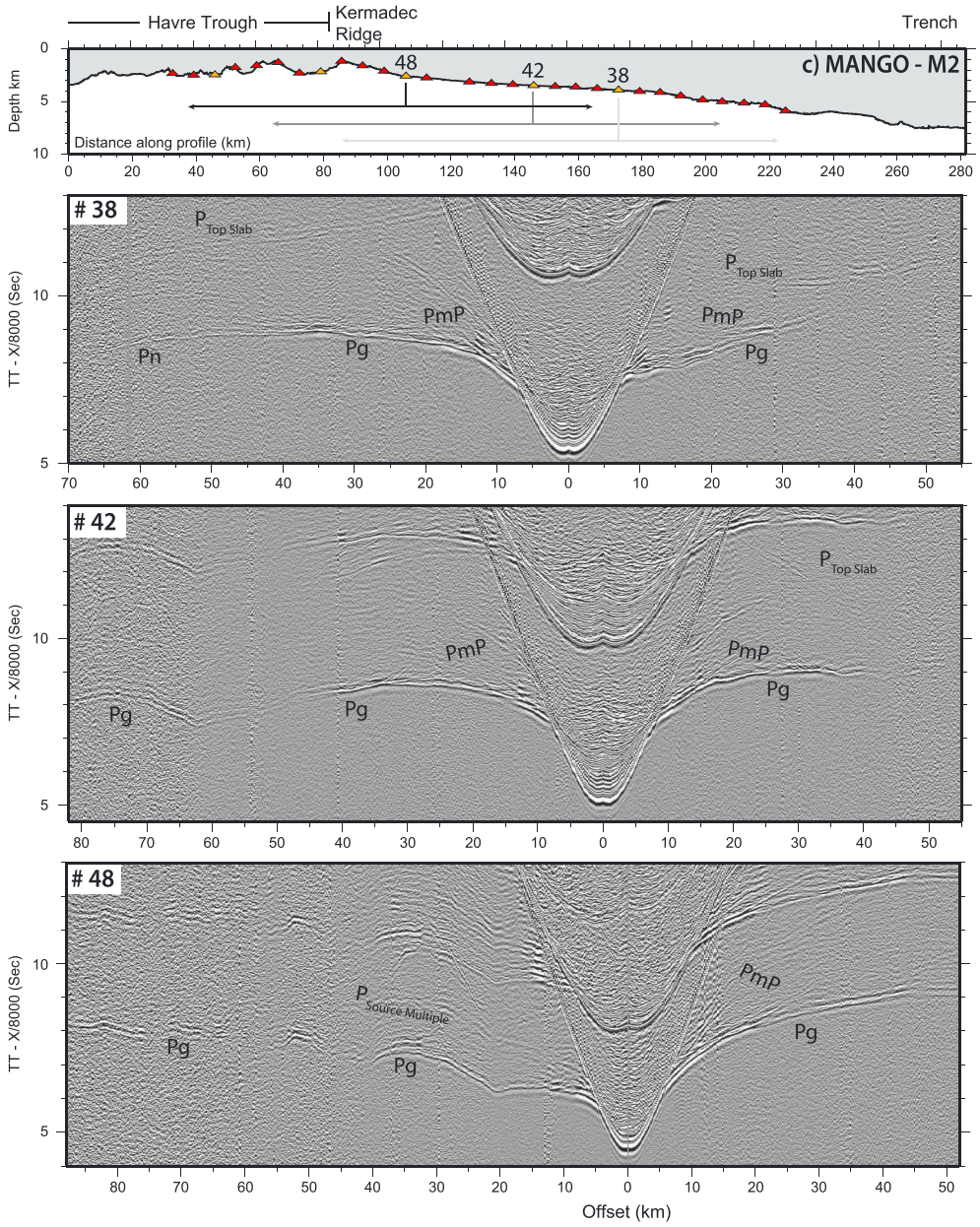

Figure 3. (continued) c) Wide-angle seismic data along profile MANGO 2 (M2).

fore-arc, the geometry of the Moho, and V_P in the mantle wedge. Refractions through the Pacific plate and wide-angle reflections from the top and Moho of the Pacific plate constrain the geometry and seismic velocity structure of the subducting slab.

4.2. Model Limitations and Fit to Data

At the conclusion of forward modeling, outstanding travel time residuals are minimized by performing a damped least squares optimization [*Lutter et al.*, 1990; *Zelt and Smith*, 1992]. The optimization was performed until the updated model failed an *F* test (95% level) comparing the chi-square (χ^2) value with that of the previous model.

The uncertainty in V_P is estimated by applying velocity perturbations in the form of alternating 40 km wide vertical stripes of $V_P \pm 0.4\ \mathrm{km\ s^{-1}}$ to the final optimized model (see supporting information Figures S2, S5, and S8). Following the same procedure implemented to minimize travel time residuals, a damped least

squares optimization is performed using the perturbed starting model and original travel time observations until the *F* test of model significance is failed. The difference between the final optimized and perturbed models illustrates the degree to which the final optimized model is recovered and provides a broad spatial estimate of uncertainty in V_P.

The travel time through the shallowest two layers (both Pacific and Australian plates) is constrained by the total travel times of all refracted arrivals but poorly constrained by internal turning rays. These surficial layers are therefore excluded from this uncertainty analysis, which shows V_P in most of the crust away from model end points to be constrained within $\pm 0.1\,\mathrm{km\,s^{-1}}$ (supporting information Figures S2, S5, and S8). We observe a monotonic and approximately exponential reduction in RMS and χ^2 throughout the perturbed optimization and note a strong correlation between regions of high-ray density and regions where the optimized velocity model is well recovered (see supporting information). We consider regions where the final optimized and perturbed models differ by $>0.2\,\mathrm{km\,s^{-1}}$ or have <20 rays within a 500 m search radius to be unconstrained and we apply a grey mask to differentiate these model regions.

This analysis is highly sensitive to the lateral distribution of velocity nodes. Although locally increased in regions of high horizontal velocity gradients, node spacing is ~20 km and approximately 3 times the station distribution. The horizontal resolution of these velocity models is thus limited by the distribution of velocity nodes to a range almost certainly below the full horizontal resolution given the source receiver geometry. Our objective, however, is to resolve the broad architecture of the plate margin and we are confident the large structures we interpret (20–>100 km in width) are below the horizontal resolution of both the data and model parameterization, as is confirmed by model recovery tests.

5. Results

Forward models of the seismic velocity structure along wide-angle profiles M4, M3, and M2 are presented in Figures 4–6. The data constraining these models, interpreted arrivals, and raypaths through the model for stations marked by yellow triangles are shown in the supporting information Figures S3, S6, and S9.

5.1. North-Kermadec Transect: MANGO 4

Profile M4 is dip parallel and traverses the northern Kermadec margin ~400 km south of the Louisville collision zone (Figure 1). This profile is 488 km long, extending 100 km across the Pacific plate and across the full width of the fore-arc, arc, and Havre Trough back-arc on the Australian plate. A 43 km gap in OBS/H deployments is present where the trench depth exceeded 6000 m and 57 OBS/H recorded data suitable for seismic modeling.

Seaward of the trench, the crust of the Pacific plate is modeled as a single layer 6 ± 1 km thick with V_P 6.0–7.2 $\mathrm{km\,s^{-1}}$, overlain by ~1 km of lower velocity (V_P 1.9–5.0 $\mathrm{km\,s^{-1}}$) strata (Figure 4b). The thickness of the crust and geometry of the Moho are well constrained by wide-angle reflections and refracted arrivals turning below the Moho with reversed offsets up to 70 km (Figure 3a, #96). The Pacific plate mantle is characterized by V_P 7.5–7.6 $\mathrm{km\,s^{-1}}$, but this is reduced by ~0.2 $\mathrm{km\,s^{-1}}$ within 50 km of the trench-axis where seafloor roughness increases and horst and graben structures offset the seabed. A horst block seaward of the trench is ~15 km wide, flanked by 7–8 km wide and >1.5 km deep grabens. Exposed fault scarps are >2.8 km long and dip $29 \pm 2°$. The graben defining the trench-axis has an eastern fault scarp >3.5 km long with 1.8 km of throw. Wide-angle reflections constrain the geometry of the subducting Pacific plate to ~25 km depth. The Pacific plate dips ~8° between the trench and ~19 km depth, where slab dip increases to 18°. This kink is just below the subducting slab-fore-arc Moho intersection and occurs ~10 km arcward of the transition in seismic structure and trench slope gradient separating the inner trench slope from the outer fore-arc. Wide-angle reflections are predominantly unreversed so this geometry may vary by several degrees.

The outer fore-arc has a surface gradient of 5–6° within 40 km of trench-axis and intermediate crustal velocities (5.0–5.5 $\mathrm{km\,s^{-1}}$) are capped by 1–2 km of lower velocity (V_P 1.9–4.5 $\mathrm{km\,s^{-1}}$) strata (Figure 4b). Refracted raypaths turn within 5 km of the seabed, and the crust directly overlying the subduction interface is only sampled by wide-angle reflections and P_n refractions turning within the Pacific plate (Figure S1). The outer fore-arc contains at least two bathymetric and crustal ridges, separated by 7–8 km wide basins containing thicker (factor ≥ 2) sedimentary sequences. These structures may reflect the surface

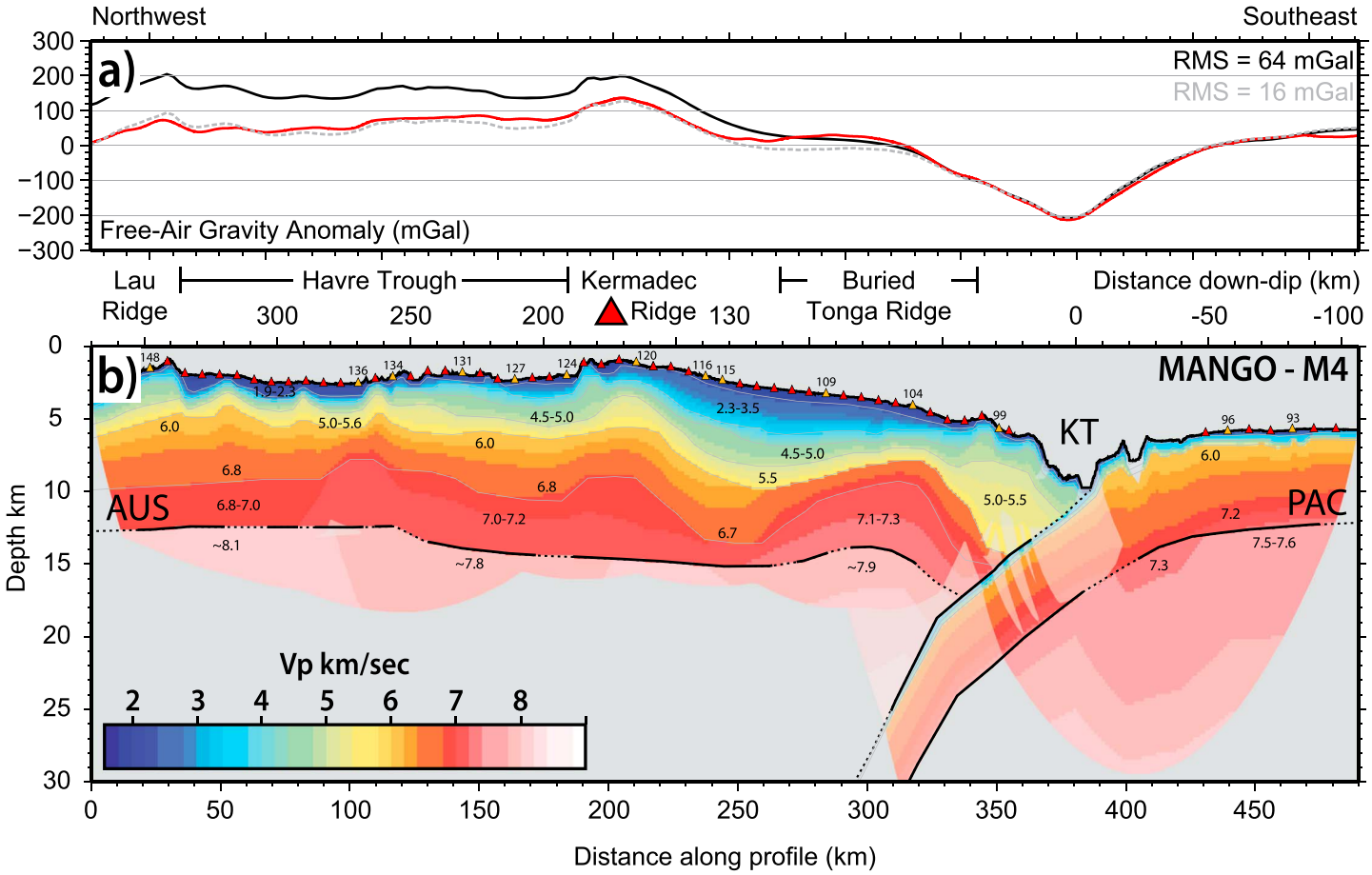

Figure 4. (a) Free-air gravity anomaly (red line) observed along Profile M4. Solid black line shows the free-air gravity anomaly calculated from the seismic velocity model above 18 km depth with the grey dash showing the calculated anomaly incorporating contributions from the subducting slab and mantle wedge. (b) Dip-parallel seismic velocity (V_P) structure along Profile M4. Solid (dotted) black lines distinguish regions where crustal interfaces are (are not) constrained by wide-angle reflections. Transparent mask shows regions unconstrained by refracted raypaths or with V_P uncertainty >0.2 km s^{-1}. Solid grey mask defines the limits of full ray coverage. Numbers give P wave velocities in km s^{-1}. Ocean Bottom Seismographs are marked by triangles. Large red triangle marks the volcanic arc. Record sections, interpretations, and associated raypaths for OBS/H marked by yellow triangles (station numbers labeled) are shown in the supporting information Figure S3. Annotations: KT = Kermadec Trench; PAC = Pacific Plate; and AUS = Australian Plate.

expression of subducting horst and grabens, but resolution in the subducting crust is insufficient to identify these structures at depth.

The inner fore-arc is characterized by a shallow 1.7° trench-slope gradient, an east-west increase in the thickness of low-velocity sediments and a significant increase lower crustal V_P (Figure 4b). Surficial sediments (V_P 1.9–4.3 km s^{-1}) thicken east to west from 1.5 to 3.8 km and are underlain by a farther 2–3 km of strata with V_P 4.5–5.5 km s^{-1} forming an asymmetric seaward tilted basin. Lower crustal velocities are inversely correlated with the thickness of basin fill and crustal wavespeeds reach the shallowest depth and are fastest (6.5–7.3 km s^{-1}) in the east, generating steep horizontal velocity gradients between the inner and outer fore-arc.

The geometry of the Moho and mantle wedge V_P is constrained by wide-angle reflections and P_n refractions with reversed offsets of 50–100 km (Figure S3g). Moho depth increases from 14.5 km beneath the volcanic arc to ~17 km at its junction with the subducting slab. The Moho appears locally elevated beneath the region of highest lower crustal velocities, but this geometry is uncertain. The mantle wedge constrained by reversed P_n indicates V_P of 7.8–8.0 km s^{-1}.

Along M4 the active volcanic arc is coincident with the Kermadec Ridge (150–185 km from the trench-axis). The ridge is well sampled by numerous P_g phases supporting a reduction in the thickness of surficial low-

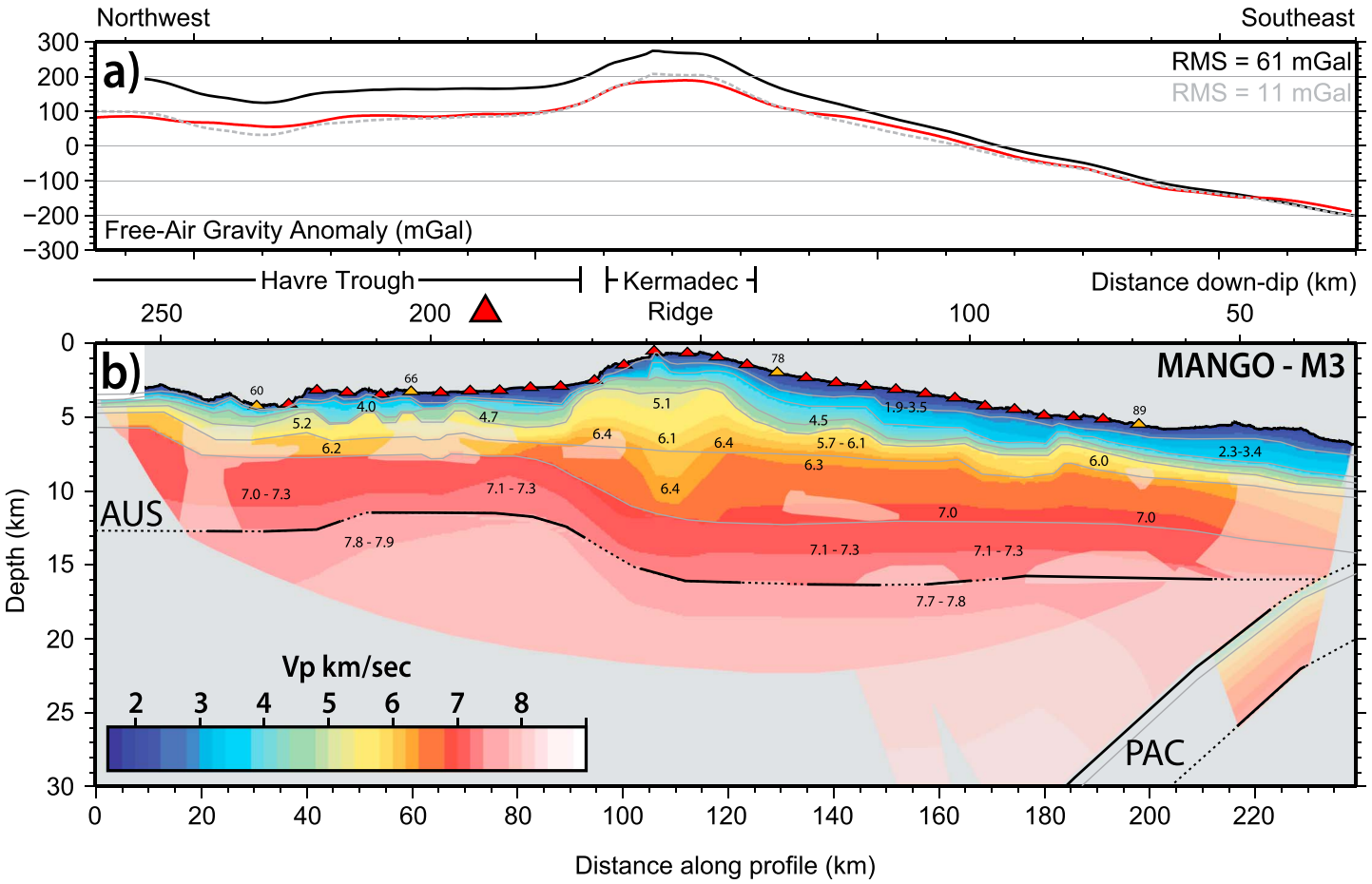

Figure 5. (a) Free-air gravity anomaly (red) observed along Profile M3. Solid black line shows the free-air gravity anomaly calculated from the seismic velocity model above 23 km depth with the grey dash showing the calculated anomaly incorporating contributions from the subducting slab and mantle wedge. (b) Dip-parallel seismic velocity (V_P) structure along Profile M3. Figure nomenclature as in Figure 4b. Record sections, interpretations, and associated raypaths for OBS/H marked by yellow triangles (station numbers labeled) are shown in the supporting information Figure S6.

velocity (V_P 1.9–4.2 km s^{-1}) strata and elevated crustal velocities. Between 2 and 5.5 km depth, V_P is 4.7–6.0 km s^{-1} and approximately 1 km s^{-1} faster than adjacent regions at equivalent depth (Figure 4b). The lower crust has V_P 6.1–7.2 km s^{-1}. We do not resolve any variation in Moho depth beneath the arc, which is ~14.5 km. Mantle wedge V_P is ~8.0 km s^{-1} but is 0.2 km s^{-1} slower over a 100 km wide region west of the arc front.

The structure of the Havre Trough back-arc basin can be centrally divided into two ~75 km wide domains. In the eastern segment, sediments (V_P 1.9–4.3 km s^{-1}) increases in thickness from 1 km near the western segment margin to ~2 km within a 25 km wide basin west of the volcanic arc. Iso-velocity contours dip 1–2° toward the arc front and crustal velocities are similar to those resolved beneath the arc. The Moho dips ~1° east, increasing in depth from ~13.5 to 15 km. Refractions turning within the mantle wedge (P_n) are interpreted across this segment (Figure S3k), but these are not widespread and are often unreversed and associated with larger uncertainties (up to 200 ms). V_P within the mantle wedge is ~7.8 km s^{-1}. Seafloor morphology is rough and blocky, characterized by a deep, steep-sided basin in the east and at least 5 small (>5 km × 500 m), pointed bathymetric highs in the west, which likely represent volcanic cones.

The western segment of the Havre Trough is defined at shallow depth by three ~1.5 km deep ~20 km wide basins. The majority of basin fill has V_P 1.9–2.3 km s^{-1} and the comparatively low signal-to-noise ratio of data across the western Havre Trough may reflect high attenuation of basin infill (Figures S3m and S3n). Basins are separated by three 1–1.5 km structural highs that persist in the seismic velocity structure to at least 6 km

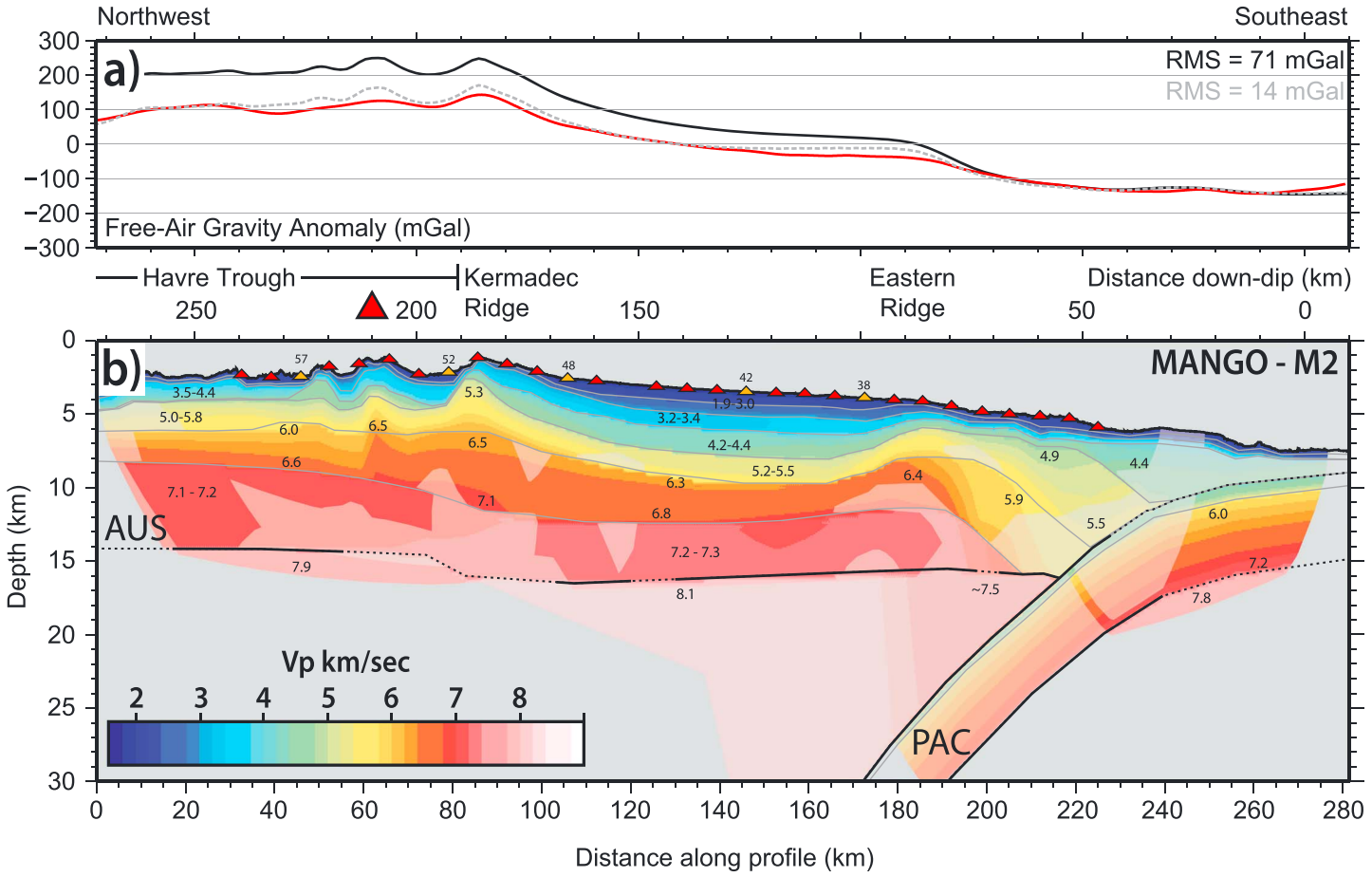

Figure 6. (a) Free-air gravity anomaly (red) observed along Profile M2. Solid black line shows the free-air gravity anomaly calculated from the seismic velocity model above 20 km depth with the grey dash showing the calculated anomaly incorporating contributions from the subducting slab and mantle wedge. (b) Dip-parallel seismic velocity (V_P) structure along Profile M2. Figure nomenclature as in Figure 4b. Record sections, interpretations, and associated raypaths for OBS/H marked by yellow triangles (station numbers labeled) are shown in the supporting information Figure S9.

depth. The easternmost high defines the eastern segment margin. The lower crust has V_P 6.0–7.0 km s^{-1}. The Moho beneath the western Havre Trough is planar and ~12.5 km deep. This geometry is predominantly constrained by wide-angle reflections, but it is also consistent with P_n refractions recorded near the segment margins. V_P within the mantle wedge is 8.1 km s^{-1}. The western Havre Trough is ~300 m deeper than the eastern segment, and back-arc structures are completely blanketed by low V_P sediments.

The Lau Ridge is a >35 km wide asymmetric structural high with V_P 1.9–5.6 km s^{-1} within 3.5 km of the seabed. The eastern ridge flank dips 15° east along a ~10 km long scarp, which defines the western margin of a sedimentary basin and the Havre Trough. The western ridge flank dips ~5° west, sediment thicknesses increase east to west, and V_P in the middle and lower crust is similar to the eastern Havre Trough. We do not seismically resolve any change in Moho depth beneath the Lau Ridge, but resolution near profile end points is low and we note than an increase in crustal thickness would improve the fit with observed gravity anomalies.

The velocity model for M4 is constrained by ~52,000 arrivals and fits these observations with RMS misfit = 0.103 s (Figure 7a).

5.2. Central-Kermadec Transect: MANGO 3

Profile M3 is dip parallel, 238 km long with 30 OBS/H deployed across the inner fore-arc, and the eastern 100 km of the Havre Trough back-arc (Figure 1). Although shooting started ~30 km from the trench-axis,

the fore-arc east of OBS/H 89 is only constrained by unreversed refractions and wide-angle reflections therefore the outer fore-arc is not well constrained (Figure 5a).

The inner fore-arc has a mean surface gradient of 2.5° and, in contrast to profile M4, is structurally homogeneous east of the Kermadec Ridge. Within 2 km of the seabed, sediments have V_P 1.9–3.5 km s^{-1} and are underlain by 1.5–2 km of strata with V_P 3.6–5.0 km s^{-1}. Crustal wave speeds increase from 5.7 to 7.3 km s^{-1}. Moho geometry and mantle wedge V_P are constrained by wide-angle reflections and by refracted arrivals with reversed offsets of up to 170 km (Figures 3b #60, S6a, and S6d). The Moho is planar at ~16 km depth and the mantle wedge has V_P 7.7–7.8 km s^{-1}. The subducting Pacific plate is only constrained geometrically by wide-angle reflections and is modeled with V_P 6.0–7.2 km s^{-1} (from profile M4), ~6 km thickness and a dip of 17°. This dip may vary by several degrees as reflections are unreversed.

The Kermadec Ridge is characterized by a reduction in the thickness of surface sediments and V_P increases to 4.3 km s^{-1} within 2 km of the seabed. The upper crust is 3 km thick with V_P 4.6–5.8 km s^{-1}. In the lower crust, V_P increases from 6.0 to 7.2 km s^{-1} and lower crustal velocities occur at $<$6 km depth within two 15 km wide regions beneath the eastern and western ridge flanks, which are separated by a region of lower (by $\geq$0.4 km s^{-1}) velocity (Figure 5b).

In the eastern Havre Trough up to 1.5 km of sediment (1.9 – 3.3 km s^{-1}) has accumulated in a 20 km wide ridge-flanking basin. M3 intersects the arc front ~190 km from the trench-axis, but this intersection is ~20 km south of the nearest active volcano (Haungaroa) and the arc front is not strongly expressed bathymetrically or in the seismic structure. In the middle crust V_P increases from 5.3 to $>$7.0 km s^{-1} and V_P locally exceeds 7.3 km s^{-1} where the crust is thinnest immediately west of the Kermadec Ridge. Moho geometry and upper mantle V_P are constrained by reversed P_n refractions and by limited wide-angle reflections (Figures 3b, S6a, and S6d). These arrivals suggest a sharp reduction in Moho depth from 16.5 km beneath the Kermadec Ridge to $<$12 km beneath the eastern Havre Trough, although the precise geometry of this transition is uncertain. V_P in the arc/back-arc mantle is ~7.8 km s^{-1}.

The central Havre Trough is characterized by a reduction in both the thickness of surface sediments and lower crustal velocities (6.1–7.3 km s^{-1}). V_P exceeds 6.0 km s^{-1} within 2 km of the seabed at the western end of the profile, but refracted arrivals are limited to $<$10 km depth and the lower crust is poorly constrained. The Moho is planar at ~12.5 km depth, approximately 1 km deeper than the eastern Havre Trough.

The velocity model for M3 is constrained by ~32,000 travel times and fits these observations with RMS misfit = 0.113 s (Figure 7b).

5.3. Central-Kermadec Transect: MANGO 2

Profile M2 is dip parallel, 281 km long, and traverses the central Kermadec margin between 34 and 35°S (Figure 1). 30 OBS/H were deployed 45–240 km from the trench-axis constraining most of the fore-arc, arc, and the eastern Havre Trough (Figure 6b).

The outer fore-arc has a mean gradient of 2.2° and ~1 km of surface sediment with V_P 1.9–3.9 km s^{-1}. Crustal velocities within 40 km of the trench-axis are not well constrained, but unreversed refractions recorded by the two easternmost OBS/H suggest V_P increases to ~4.4 km s^{-1} within 2 km of the seabed. Crustal velocities 45–75 km from the trench-axis are approximately 0.6 km s^{-1} faster than the region nearer the trench, and V_P increases from 4.9 to 5.9 km s^{-1} between 2 and 7 km below the seafloor.

The geometry of the subducting slab is constrained by wide-angle reflections and dips 14° between 10 and 23 km depth and 21° between 23 and 40 km depth (supporting information Figures S7 and S9a). Refractions turning within the Pacific crust are not observed, but Moho reflections (P_mP) and P_n refractions suggest a crustal thickness of 6 km when modeled using crustal velocities resolved along M4. Unreversed P_n refractions from one OBS/H suggest V_P in the Pacific mantle is 7.8 km s^{-1}.

The inner fore-arc has a mean surface gradient of 0.5° and is characterized by a central basin bounded by fore-arc ridges. The eastern ridge (labeled in Figure 6b) is ~25 km wide and crustal velocities exceed 6.3 km s^{-1} within 3.5 km of the seabed. Sedimentary sequences thicken west of this ridge and at least 2.5 km of sediment (V_P 1.9–3.4 km s^{-1}) has accumulated in the central depocenter. Shallow sedimentary

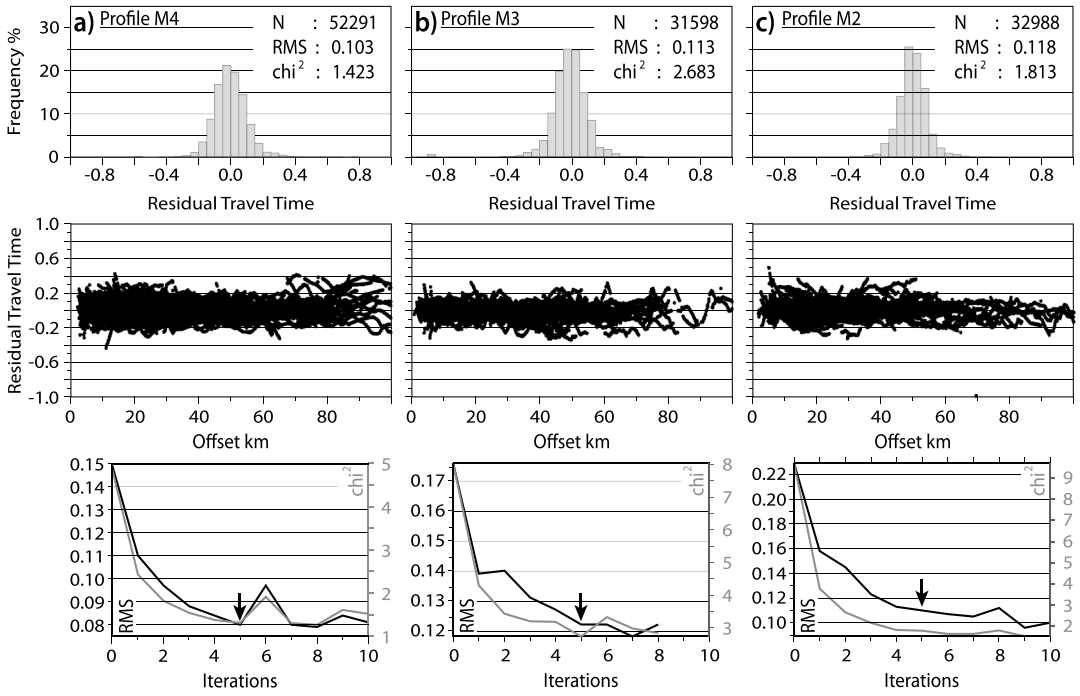

Figure 7. Distribution and offset relationship of travel time residuals ($T_{obs} - T_{calc}$) at the conclusion of forward modeling along (a) Profile M4, (b) Profile M3, and (c) Profile M2. For each model the number of travel time observations (N), RMS and chi-square (χ^2) statistic are shown. The bottom panel shows the reduction in RMS misfit and chi-square (χ^2) with each iteration of model recovery tests. The arrow marks the iteration at which the *F* test of model significance (95%) is failed. The difference between the perturbed starting model and the final optimized model at this point is shown in the supporting information Figures S2, S5, and S8 and is used to estimate the uncertainty in V_P.

sequences are underlain an additional 1.5 km thick layer with V_P 4.2–4.4 km s^{-1}, which may increase the thickness of basin fill to 4.5 km. The thickness of the upper crust (V_P 5.2–5.5 km s^{-1}) is inversely correlated with basin thickness, below which V_P increases with decreasing gradient from 6.3 to ~6.8 km s^{-1}. The lower crust is 4 km thick with V_P 7.2–7.3 km s^{-1}. The Moho is constrained by P_n refractions beneath the central basin and limited wide-angle reflections and appears to shallow from 16.5 km beneath the Kermadec Ridge to 15.5 km at the trench-slope break (Model km 190). V_P in the mantle wedge is 8.0 km s^{-1}, but wide-angle reflections suggest this may reduce by 0.3–0.6 km s^{-1} within 40 km of the mantle wedge corner.

The Kermadec Ridge is structurally and morphologically asymmetric. The eastern ridge flank dips ~4° east, iso-velocity contours parallel the seabed from the central basin and V_P is <3.8 km s^{-1} within 1.5 km of the seabed. By contrast, the western ridge flank dips 12°, sedimentary cover is less than 500 m thick and crustal wave speeds (V_P >5.0 km s^{-1}) reach the shallowest depth within a 10 km wide dome between the ridge crest and western scarp.

The active arc is located in the eastern Havre Trough and M2 traverses the caldera volcano Sonne [*Haase et al.*, 2002] 210 km from the trench-axis. Sediments (V_P 1.9–4.0 km s^{-1}) regionally exceed 1.5 km thickness and the arc front is characterized by a 0.5 km s^{-1} increase in middle crustal wave speeds. A second smaller (15 km × 700 m) cone located west of Sonne is characterized by reduced sediment thicknesses. The central Havre Trough is morphologically rougher, V_P exceeds 3.5 km s^{-1} within 500 m of the seabed and V_P increases from 5.0 to 6.6 km s^{-1} in the upper crust. Lower crustal velocities (7.1–7.2 km s^{-1}) are slightly slower than observed beneath the arc and inner fore-arc. The geometry of the Moho is constrained by wide-angle reflections and unreversed P_n refractions and is ~14 km deep, ~2 km shallower than beneath the Kermadec Ridge.

The velocity model for M2 is constrained by ~33,000 travel times and fits these observations with RMS misfit = 0.118 s (Figure 7c).

6. Gravity Models

6.1. Construction Steps

The empirical V_P-density relation from *Brocher* [2005] is used to convert forward velocity models to density, from which the 2-D gravity effect is calculated using a line integral method [*Bott*, 1965]. The R/V *SONNE* was not fitted with a gravity meter during SO192-1 and we thus compare the gravity effect of crustal models to free-air gravity anomalies derived from satellite altimeter data (Figures 4a, 5a, and 6a) [*Sandwell and Smith*, 1997, 2009; *Sandwell et al*., 2014]. A comparison between shipboard and altimeter-derived gravity measurements along the full length (10,725 km) of the R/V *SONNE* SO215 ship track [*Peirce and Watts*, 2011] shows the satellite derived gravity field offset slightly (~4 mGal) to higher values, but this discrepancy and the RMS misfit (7 mGal) are small in comparison to the amplitude of variations in free-air gravity anomalies across the fore-arc (>250 mGal).

The maximum depth of refracted raypaths along Profile M2 is ~20 km, but V_P in the mantle wedge is constrained and wide-angle reflections constrain the geometry and approximate thickness of the subducting slab to at least 25 km depth (supporting information Figure S7). The free-air gravity anomaly predicted from the crustal structure above this depth fits the observed gravity field with an RMS misfit of 71 mGal. Profiles M4 and M3 are well constrained to ~18 km and ~23 km depth and calculated free-air gravity anomalies fit the observed gravity field with RMS misfits of 64 mGal and 61 mGal, respectively. Gravity anomalies along PA are incorporated from *Stratford et al*. [2015].

As is often observed in subduction zones, calculated free-air gravity anomalies of the seismically constrained crustal structure are offset to higher values with increasing distance landward of the trench. For example, the predicted gravity anomaly at the western end of M4 is ~140 mGal higher than the observed free-air anomaly (Figure 4a). Correcting for differences in profile geometries by plotting outstanding gravity residuals against distance from the trench, we note a systematic misfit across all four profiles distributed along ~1100 km of the Tonga-Kermadec margin between 25°S and 35°S (Figure 8a). This misfit is typically small (<50 mGal) with a shallow gradient within ~75 km of the trench then steepens to a maximum gradient of ~1.0 mGal/km at trench distances of 100–180 km, before shoaling in gradient and flattening at 100 ± 20 mGal at trench distances >180 km. These residuals are outstanding after the gravity contribution calculated from the crustal structure has been removed and their systematic long-wavelength form suggests that they likely reflect gravity contributions from differences in the structure of the subducting slab and/or mantle wedge seaward and landward of the trench-axis [*Scherwath et al*., 2010; *Contreras-Reyes et al*., 2011; *Stratford et al*., 2015].

We consider these gravity contributions separately by constructing simple 2-D bodies. The top of the subducting slab is constrained at ≤30 km depth by forward velocity models and at greater depth (up to 400 km) by SLAB-1.0 [*Hayes and Wald*, 2009; *Hayes et al*., 2012]. The base of the subducting lithosphere is fixed 70 km below the subduction interface. The mantle wedge body is restricted to depths ≥20 km, above which the gravity contribution from crustal models has been calculated and removed. This simple parameterization has four remaining variables, which are the density contrasts associated with the slab ($\Delta\rho_{slab}$) and mantle wedge ($\Delta\rho_{wedge}$), the minimum depth of the slab anomaly (z_{slab}), and the maximum depth of the mantle wedge anomaly (Z_{wedge}). These parameters are determined simultaneously by performing a least squares optimization. We use the RMS misfit between the shallow crustal gravity residual and the combined gravity anomaly associated with the slab and mantle wedge bodies across four dip-parallel wide-angle profiles (PA, M4, M3, and M2 Figure 1) as our metric of fit and use a downhill simplex method to find the best fitting parameters, $\Delta\rho_{slab} = 0.024$ g/cm^3, $\Delta\rho_{wedge} = -0.045$ g/cm^3, $z_{slab} = 65$ km, and $Z_{wedge} = 95$ km.

Figure 8b shows that the slab anomaly (red) is characterized by a broad and shallow high (~20 mGal) centered ~150 km landward of the trench-axis. The gravity anomaly associated with low-density mantle wedge (blue) is characterized by a broad low with amplitude of up to −120 mGal, which has the steepest gradients 70–150 km from the trench. Within 70 km from the trench-axis, the near complete fit provided by shallow crustal structure requires that the gravity anomalies associated with the slab and mantle wedge approximately cancel. The combined gravitational effect of the slab and mantle wedge contributions (grey dash) fits outstanding shallow-crustal gravity residuals with an RMS misfit of 14 mGal (Figure 8b). Applying these contributions along profiles M2, M3, and M4 reduces RMS misfits to 14 mGal, 11 mGal, and 16 mGal, respectively. Most outstanding gravity residuals are located at profile end points in poorly constrained model regions (Figures 4–6).

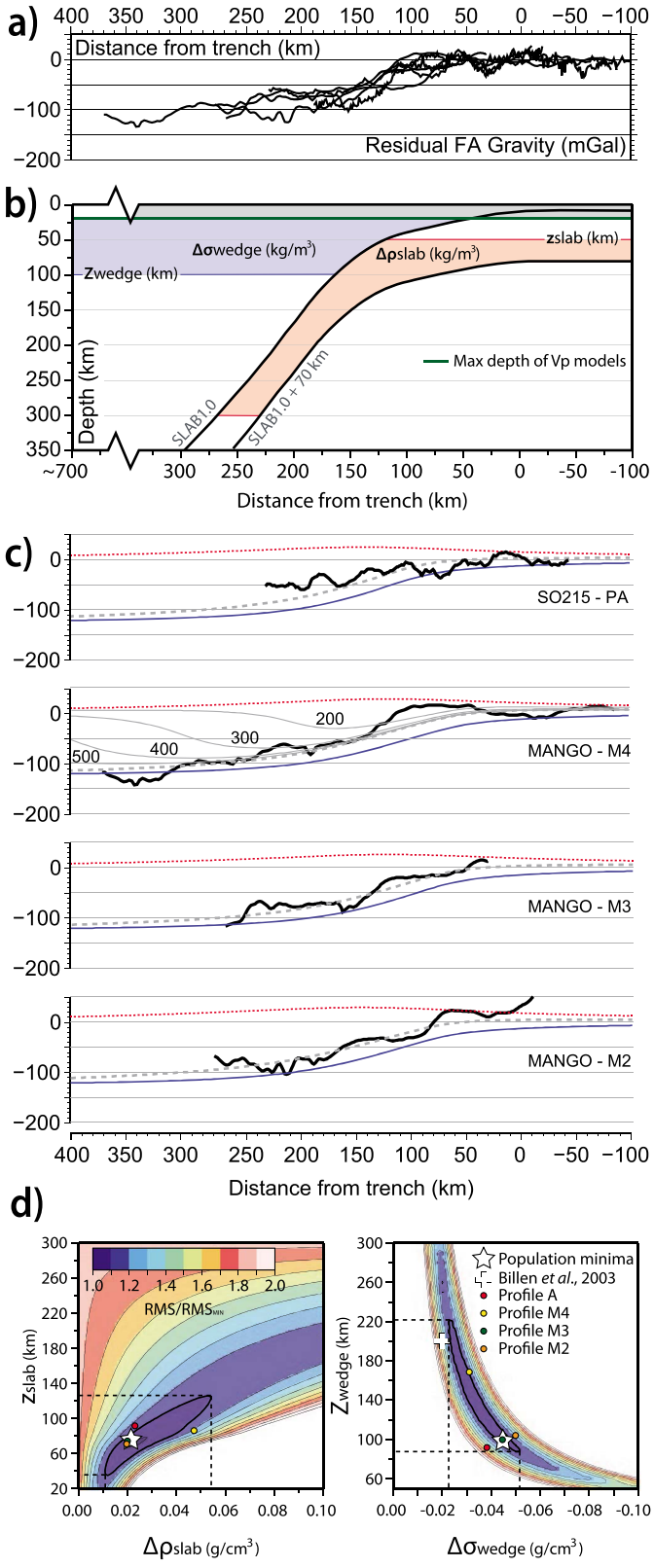

6.2. Shallow Crustal Gravity Residuals as a Constraint on Deep Structure

Dynamic models of viscous flow in subduction zones including a fault (shear zone) along the plate interface have successfully reproduced trench morphology [*Zhong and Gurnis*, 1992, 1994; *Zhong et al*., 1998; *Buiter et al*., 2001] and the long-wavelength geoid [*Zhong and Gurnis*, 1994]. Contrary to observations, these models predict a large depression (3–4 km) in dynamic topography in the arc/back-arc region and a short-wavelength depression in the geoid or gravity. *Billen and Gurnis* [2001] present the first results showing that this depression can be removed by incorporating a low-viscosity region in the mantle wedge, which effectively decouples the overthrusting plate from the flow induced in the mantle wedge by the slab.

For the Tonga-Kermadec subduction zone, *Billen et al*. [2003] use observations of strain rate, stress orientation, crustal thickness, dynamic topography, and the geoid as constraints on

Figure 8. (a) Stack of shallow-crustal free-air gravity residuals outstanding after the gravity effect of shallow crustal models for profiles PA, M4, M3, and M2 (Figure 1) has been calculated and subtracted from observed free-air gravity anomalies. (b) Cartoon illustrating the model parameterization. (c) Gravity residuals (black) and combined gravity anomalies (grey dash) associated with contributions calculated for the subducting slab (red) and mantle wedge (blue). For profile M4, solid grey lines show combined gravity anomalies varying the lateral extent of the lower density mantle wedge. (d) RMS showing the trade-off between the minimum depth (z_{min}) and density contrast (ρ_{slab}) for the slab anomaly (left) and between the maximum depth (Z_{max}) and density contrast (ρ_{wedge}) for the mantle wedge anomaly (right). White star shows the parameters simultaneously best fitting shallow-crustal residuals for all profiles with the parameters best fitting individual profiles shown as red (PA), yellow (M4), green (M3), and orange (M2) dots. White plus shows the wedge parameters determined by *Billen et al*. [2003].

viscosity and buoyancy in a 3-D finite-element model of mantle flow. They find that incorporating a low-viscosity wedge makes it possible to match observations of positive dynamic topography and horizontal extension in the back-arc and downdip compression in the shallow portion of the slab. This is the first time these observations have been reproduced by dynamic models and are shown to be a natural consequence of including a low-viscosity region in the mantle wedge. To match the observed topography, *Billen et al*. [2003] include variations in lithosphere age, crustal thickness, and a broad (≥700 km wide) low-density region ($\Delta\rho = -0.02$ g/cm^3) in the mantle wedge extending from 20 to 200 km depth.

The shallow crustal gravity residuals calculated in this study provide independent constraints on the density structure of the subducting slab and mantle wedge. For each contribution, the trade-off between the vertical extent and density contrasts is shown in Figure 8d. RMS difference is normalized with respect to the population minima (white star) and colored dots show the parameters that best fit the shallow crustal residuals along each wide-angle profile. The white cross shows the density and depth extent of the low-viscosity/density mantle wedge determined by *Billen et al*. [2003]. From the range of parameters in which RMS is within 10% of the population minima, $\Delta\rho_{slab}$ and z_{slab} are constrained to 0.01–0.055 g/cm^3 and 40–120 km, respectively, and $\Delta\sigma_{wedge}$ and Z_{wedge} are constrained to -0.022 – -0.052 g/cm^3 and 90 – 220 km, respectively (Figure 8d).

Although the best fitting density anomaly associated with the subducting slab is relatively small for a rapidly converging plate boundary, the associated minima shown in Figure 8d is broad and the range of possible density anomalies is consistent with earlier seismically constrained gravity models along the Tonga-Kermadec margin [*Scherwath et al*., 2010; *Stratford et al*., 2015] and flexural studies on the gravity effect of the subducting slab elsewhere in the Pacific [*Watts and Talwani*, 1975; *Davies*, 1981]. Holding the slab parameters at their least squares estimates, the wedge parameters ($\Delta\sigma_{wedge}$ -0.02 g/cm^3 and Z_{wedge} 200 km) determined by *Billen et al*. [2003] are located slightly outside the minima we define and RMS is ~40% higher, but this can be reduced to <20% if there is no gravity contribution from the subducting slab.

The density anomaly in the mantle wedge (-0.045 g/cm^3) likely reflects the effect of water on partial melting and the petrology of the mantle wedge. One of the primary effects of water flux is to increase the degree of melting by lowering the solidus temperature. The density anomaly we calculate is equivalent to having nine weight percent *in situ* melt with a density of 2.7 g/cm^3. This, however, is assuming a reference mantle density of 3.2 g/cm^3, which may be too high particularly at shallow depths where V_P of ~7.8 km s^{-1} suggests either minor degrees (i.e., 10–15%) of mantle serpentinization [*Christensen*, 1966, 1996; *Carlson and Miller*, 2003] or the presence of cumulate rocks below the Moho [*DeBari and Greene*, 2011; *Timm et al*., 2016]. Regions of lower density caused by high melt fraction would also be expected predominantly beneath the volcanic arc. A secondary effect of large degrees of partial melting can also reduce the density of the residue. As described by *Billen et al*. [2003], large degrees of partial melting lowers the Al_2O_3 contents of the residue, which can inhibit garnet formation if transported by flow into the garnet stability field (>3 GPa). The degree of melting in Mariana island arc magmas is >30% [*Stolper and Newman*, 1994], which *Billen et al*. [2003] calculate would lead to a density reduction of 0.01–0.02 g/cm^3 relative to peridotite subjected to only 10 wt % melting or 0.05 g/cm^3 relative to fertile peridotite. These density anomalies may not be focused beneath the active arc. Finally, at low pressures (~1 GPa) and temperatures (<600°C), serpentinization of the mantle wedge is a process common to many subduction zones [*Hyndman and Peacock*, 2003]. Along the Kermadec arc, seismic wave-speeds below the fore-arc Moho (7.7–8.1 km/s) are consistent with 10–20 vol % of serpentine (at 1 GPa) [*Christensen*, 1966, 1996; *Carlson and Miller*, 2003] and may exceed 25 vol % of serpentine within 40 km of the mantle wedge corner where V_P may be as low as 7.5 km/s (Figure 6b) [*Stratford et al*., 2015]. It is possible all three mechanisms are contributing to lowering the density of the Kermadec mantle wedge, but our simple parameterization cannot discriminate between these.

Profile M4 extends across the full width of the Havre Trough back-arc and thus constrains the minimum distance from the trench that the low-density region in the mantle wedge must extend. In Figure 8c, we show the combined gravity anomaly from the mantle wedge and subducting slab varying the maximum lateral extent of the mantle wedge anomaly between 200 km and 500 km (labeled thin grey profiles). It is not possible to match the shallow crustal residual along M4 unless the low-density mantle wedge extends >500 km from the trench and this residual is best fit by lateral extents >700 km. This width is consistent with

Billen et al. [2003] who extend the low-density mantle wedge ~850 km from the trench-axis in order to match the bathymetry of the South Fiji Basin. These observations suggest that low-density/viscosity regions created within the mantle wedge are laterally decoupled and left behind as the trench retreats and the slab rolls back, which is consistent with their role in vertically decoupling the overthrusting plate from the negative buoyancy force of the subducting slab. We suggest that the shallow crustal residuals described above provide independent and complementary evidence of a broad, low-density (and low-viscosity) wedge beneath the central Tonga-Kermadec arc and the back-arc basin that flanks it to the west [*Billen et al*., 2003].

7. Spectral Averaging of the Regional Gravity Anomalies and Bathymetry

Subduction fore-arcs are characterized by steep topographic and gravimetric gradients with global averages showing ~6.0 km of relief and a ~200 mGal increase in free-air gravity anomalies across the 100 km landward of the trench-axis. To isolate shorter wavelength and lower amplitude structure that may be masked by these gradients, *Bassett and Watts* [2015a, 2015b] and *Bassett et al*. [2016] have developed a method for calculating and then removing spectral averages of the trench normal topographic and gravimetric profile from regional grids of bathymetry [*Intergovernmental Oceanographic Commission (IOC) et al*., 2003] and free-air gravity anomalies [*Sandwell and Smith*, 1997; *Smith and Sandwell*, 1997; *Sandwell and Smith*, 2009].

We have applied this method of spectral averaging to isolate the gravimetric expression of the Tonga Ridge (Figure 9). The bathymetric expression of the ridge is strongest north of 26°S, but gravity data derived during the GEOSAT altimeter mission suggest a buried southward continuation of the Tonga Ridge may extend as far south as 31°S [*Collot and Davy*, 1998]. Hence, we subtract an ensemble average profile calculated across the southern Kermadec arc (35°S–31°S). Residual free-air gravity anomalies clearly reveal the buried southward extension of the Tonga Ridge (Figure 9b). The gravimetric expression is strongest ($>$100 mGal) north of 25°S but is contiguous in form, maintains a residual amplitude $\geq$50 mGal, and has a width (110 $\pm$ 20 km) consistent with the well-resolved northern segment as far as 30.5°S. In contrast to the trench and arc parallel northern segment, south of 25°S the ridge strike is approximately north-south (~006°) and appears more closely matched geometrically with the eastern margin of the Lau Ridge than the trench-axis.

8. Along-Strike Variations in Crustal Structure

8.1. Structure and Latitudinal Extent of the Tonga Ridge

The detailed structure of the Tonga-Kermadec fore-arc between ~27°S and ~38°S, as constrained by five wide-angle refraction profiles, is shown in Figure 10. North of ~31°S, the fore-arc is occupied by the buried Tonga Ridge and a strong correlation is observed between the residual gravimetric expression of the ridge (dashed in grey) and regions of higher crustal velocities (V_P 6.9–7.3 km s^{-1}). The arc front is located west of the Tonga Ridge, forming the active Kermadec Ridge. At the latitude of PA, the offset between these ridges is $<$30 km and is only apparent from the residual free-air gravity anomaly (Figure 10a) and a slight deepening of iso-velocity contours between the active arc (red triangle) and the eastern high-velocity crest of the Tonga Ridge (Figure 10b) [*Stratford et al*., 2015]. Farther south at the latitude of M4, the distance between the Tonga and Kermadec Ridges has increased to 60–70 km. Both ridges are clearly resolved as regions of elevated crustal wave speeds and up to 4 km of sediments (V_P 1.9–4.3 km s^{-1}) of likely volcaniclastic origin have accumulated in the intervening basin. These sediments generate a smooth fore-arc trench slope, thereby preventing the separation of active and extinct arc ridges from being expressed bathymetrically.

Supporting the inference from residual free-air gravity anomalies that the Tonga Ridge does not extend beyond ~30.5°S, the seismic velocity structure along M3 is homogeneous with iso-velocity contours broadly parallel to the seabed between the Kermadec Ridge and the trench. Thinner sediment volumes and the absence of a centralized fore-arc basin are consistent with the positive nature of residual gravity anomalies east of the Kermadec Ridge (Figure 9b). Lower crustal velocities along M3 are only marginally slower (6.0–7.2 km s^{-1}) than observed beneath the Tonga Ridge, which is thus seismically defined by higher V_P (locally up to 0.8 km s^{-1} faster) at intermediate depth (3–8 km below seabed), the shallow westward dip of iso-velocity contours beneath the ridge platform and the sharp reduction in V_P beyond the eastern ridge flank.

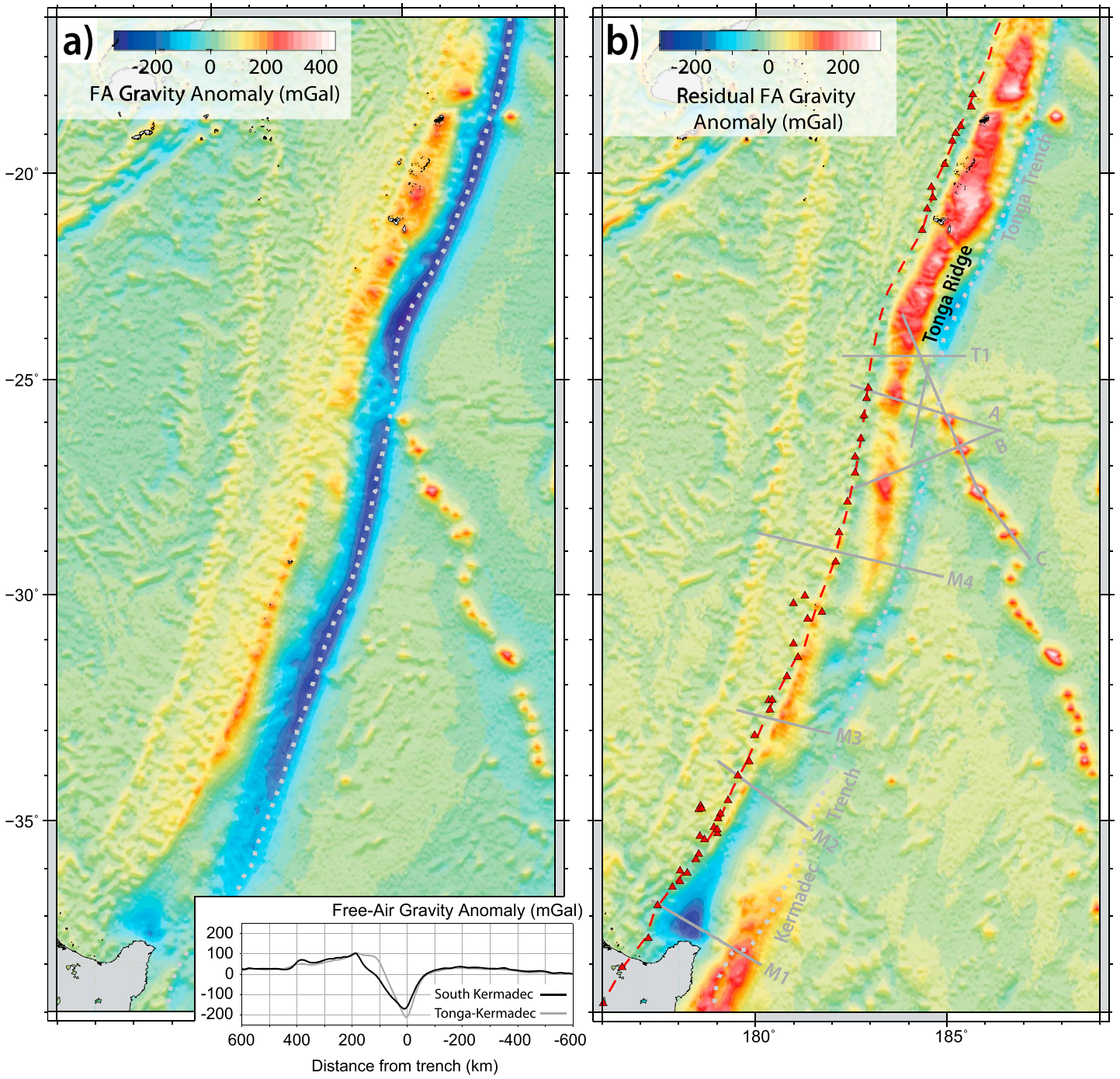

Figure 9. (a) Free-air gravity anomalies calculated from satellite altimetry [*Sandwell and Smith*, 1994, 1997, 2009]. Grey dashed line marks the trench-axis. Insert shows the ensemble average trench-normal profile calculated along the southern Kermadec margin (black) and full length of the Tonga-Kermadec margin (grey). (b) Residual free-air gravity anomalies calculated by subtracting the southern Kermadec ensemble average. Grey lines show wide-angle seismic profiles. Red triangles and dashed line show arc volcanoes and the arc axis, respectively.

Profile M2 is located at the northern tip of the Raukumara Plain. The fore-arc is characterized by a central 4.5 km deep basin bounded by fore-arc ridges. This basin may be contiguous with the deeper Raukumara Basin resolved by MCS data [*Sutherland et al.*, 2009] and M1 refraction data [*Scherwath et al.*, 2010]. The crustal thickness underlying the central basin (6–7 km) is comparable to Raukumara Basin, although crustal velocities are faster along M2 [*Bassett et al.*, 2010; *Scherwath et al.*, 2010]. The ridge bounding the basin to

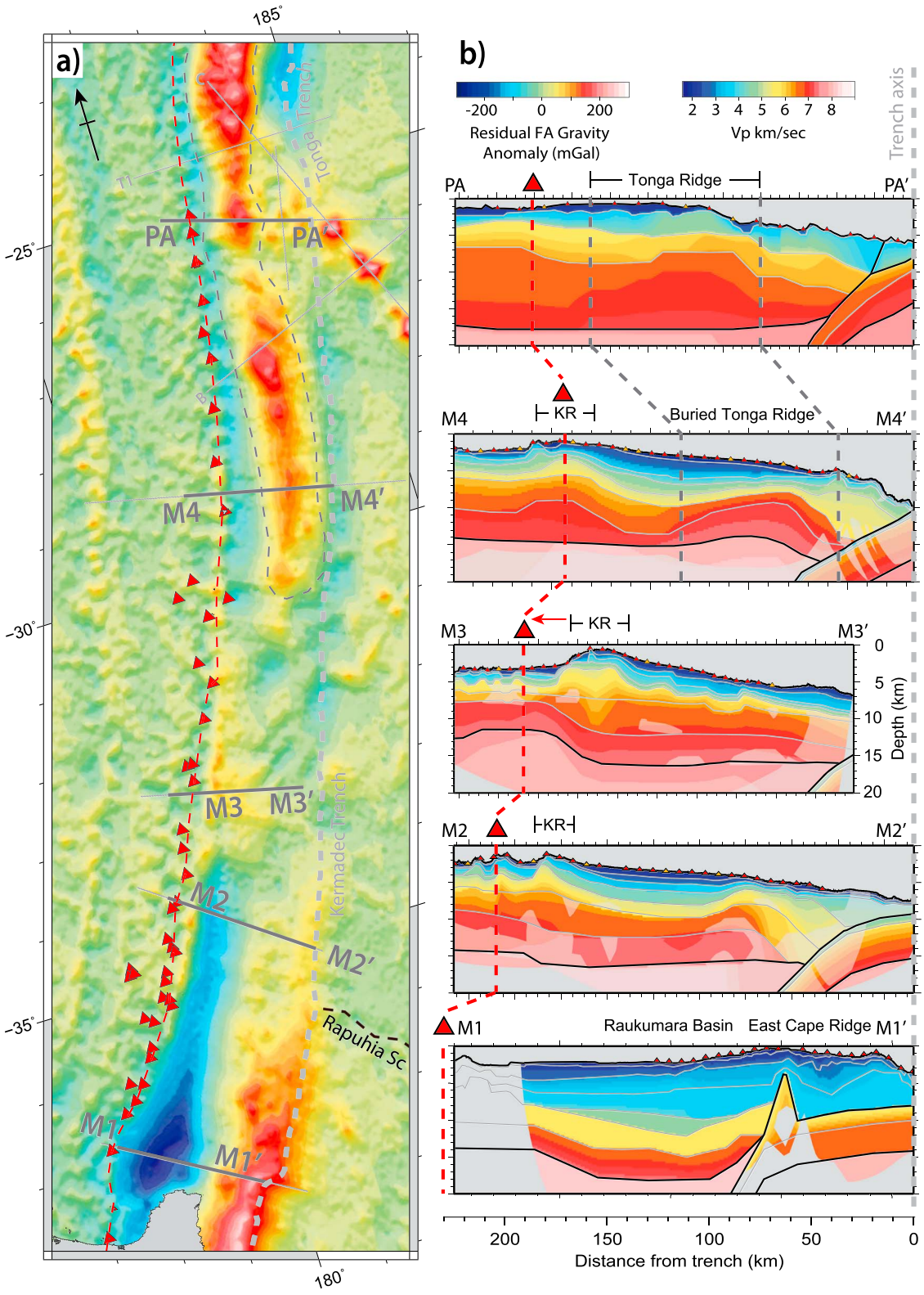

Figure 10. (a) Residual gravity anomaly and (b) fore-arc crustal structure. Forward velocity models are plotted against distance from the trench. Profile M1 is from *Scherwath et al.* [2010]. Profile PA is from *Stratford et al.* [2015]. Seismic models are plotted against distance from the trench. Mask shows unconstrained model regions. Light grey, dark grey, and red dashed profiles (with triangles) show the trench axis, our interpreted geometry for the Tonga Ridge and the location of the active volcanic arc front, respectively. Note the association of higher seismic velocities in the fore-arc with large positive residual free-air gravity anomalies and the relatively smooth fore-arc structure along profile M3.

the east also appears gravimetrically contiguous with the East Cape Ridge (Figure 9). The step in bathymetry and free-air gravity anomalies along the frontal ridge is coincident with the Rauphia Scarp and most likely reflects the increased crustal thickness and shallower bathymetry of the subducting Hikurangi Plateau (Figure 10a). The velocity structure of East Cape Ridge is constrained by 2-D OBS/H and 3-D onshore-offshore wide-angle refraction experiments [*Bassett et al*., 2010; *Scherwath et al*., 2010]. In contrast to the velocity structure of the Tonga Ridge (Figure 10b), the majority of the East Cape Ridge is characterized by $V_P < 4\,\mathrm{km\,s^{-1}}$. Basement velocities (4.9–7.2 $\mathrm{km\,s^{-1}}$) at intermediate depths beneath the East Cape Ridge crest appear related to Raukumara Basin basement uplifted above a low-velocity (3.5–5.0 $\mathrm{km\,s^{-1}}$) prism located above the subducting Pacific plate. This low-velocity anomaly can be tracked in tomographic V_P models beneath the Raukumara Ranges and is interpreted as underplated sedimentary and crustal material [*Bassett et al*., 2010].

8.2. Arc and Back-arc Structure Across the 32°S Boundary

Along-strike variations in the structure of the arc and back-arc have been predominantly recognized from bathymetry and gravity observations [*Pelletier and Dupont*, 1990; *Wright*, 1997; *Ballance et al*., 1999; *Delteil et al*., 2002; *Wright et al*., 2006; *de Ronde et al*., 2007; *Timm et al*., 2014]. Figure 11 shows four wide-angle models that provide the first regional seismic constraints on the crustal structure of the volcanic arc and Havre Trough between 35°S and 25°S.

North of 32°S the active arc front is located on the Kermadec Ridge and is characterized by a ~30 km wide region with higher wave speeds (by ~0.5 $\mathrm{km\,s^{-1}}$) within 7 km of the seabed. Moho depth beneath the arc is 17 km along PA and 15 km along M4. The bathymetric ridge hosting the volcanic arc is >200 km wide between 26°S and 24.5°S and the active arc along PA is weakly expressed by a reduction in sediment thickness and an east-west shoaling of iso-velocity contours from the Tonga Ridge [*Stratford et al*., 2015].

Profile M4 traverses the full width of the Havre Trough and shows two structural domains of ~75 km width. The eastern Havre Trough is structurally homogeneous. Shallow sedimentary and upper crustal layers thicken toward the arc and the lower crust has V_P 6.0–7.2 $\mathrm{km\,s^{-1}}$. The Moho dips east from 13.5 to 14.5 km and a mean seafloor depth of ~1.9 km yields a crustal thickness of ~12 km (including sediments). The western Havre Trough, in contrast, shows more complex structure and three ~1.5 km deep ~20 km wide basins are separated by structural and V_P highs. These highs may be fault controlled extrusive volcanic ridges or horst-graben fault blocks, possibly containing rifted fragments of the Lau Ridge. Relative to the eastern Havre Trough, the upper crust (V_P 4.6–6.0 $\mathrm{km\,s^{-1}}$) is thinner (~1 km thick) and the lower crust is slower. The Moho is ~12.5 km deep and mean seafloor depth of ~2.4 km yields a crustal thickness of ~10 km, which is 2 km thinner than the eastern segment. Seismic structure is correlated with seafloor morphology and the contrast between the high-standing, rugged eastern segment with the smooth and deeper western segment extends this structural division (dashed grey line in Figure 11a (M4) and 11b) at least as far north as 26°S. This extension is supported by the similar velocity structure, Moho depth, and crustal thickness resolved in the western Havre Trough but 400 km north of M4 near ~26°S by *Nishizawa et al*. [1999].

South of 32°S the volcanic arc is located in the eastern Havre Trough. In contrast to the seismic structure of the arc-high north of 32°S, the Kermadec Ridge along M3 and M2 is structurally asymmetric with the fastest wave speeds located beneath the western ridge flank. The Kermadec Ridge is also narrower (<40 km in contrast to >75 km north of 32°S), has a different trend (025° versus 018°), and the scarp facing the Havre Trough is ~2.5 km high, a factor >2 larger than that observed farther north [*Ballance*, 1999]. Moho depths beneath the Kermadec Ridge are similar along-strike (i.e., 16 ± 1 km). At shallow depth the velocity structure of the eastern Havre Trough is similar to that observed along M4, but the upper crust is thinner south of 32°S with wave speeds exceeding 6.5 $\mathrm{km\,s^{-1}}$ within 4 km of the seabed. Moho depths in the Havre Trough are inversely correlated with water depth (Figure 11a inset) with the thinnest crust (i.e., 8–9 km) observed along M3 where the Moho and mean water depth are 11.5 km and >3 km, respectively. Moho depth is less well constrained along M2, but the 14 km depth is similar to the 13–14 km depth resolved farther south and west of Raukumara Basin [*Bassett et al*., 2010]. In contrast to the central and southern segments of the Kermadec margin, no significant variation in Moho depth is observed between the fore-arc and eastern Havre Trough north of 32°S.

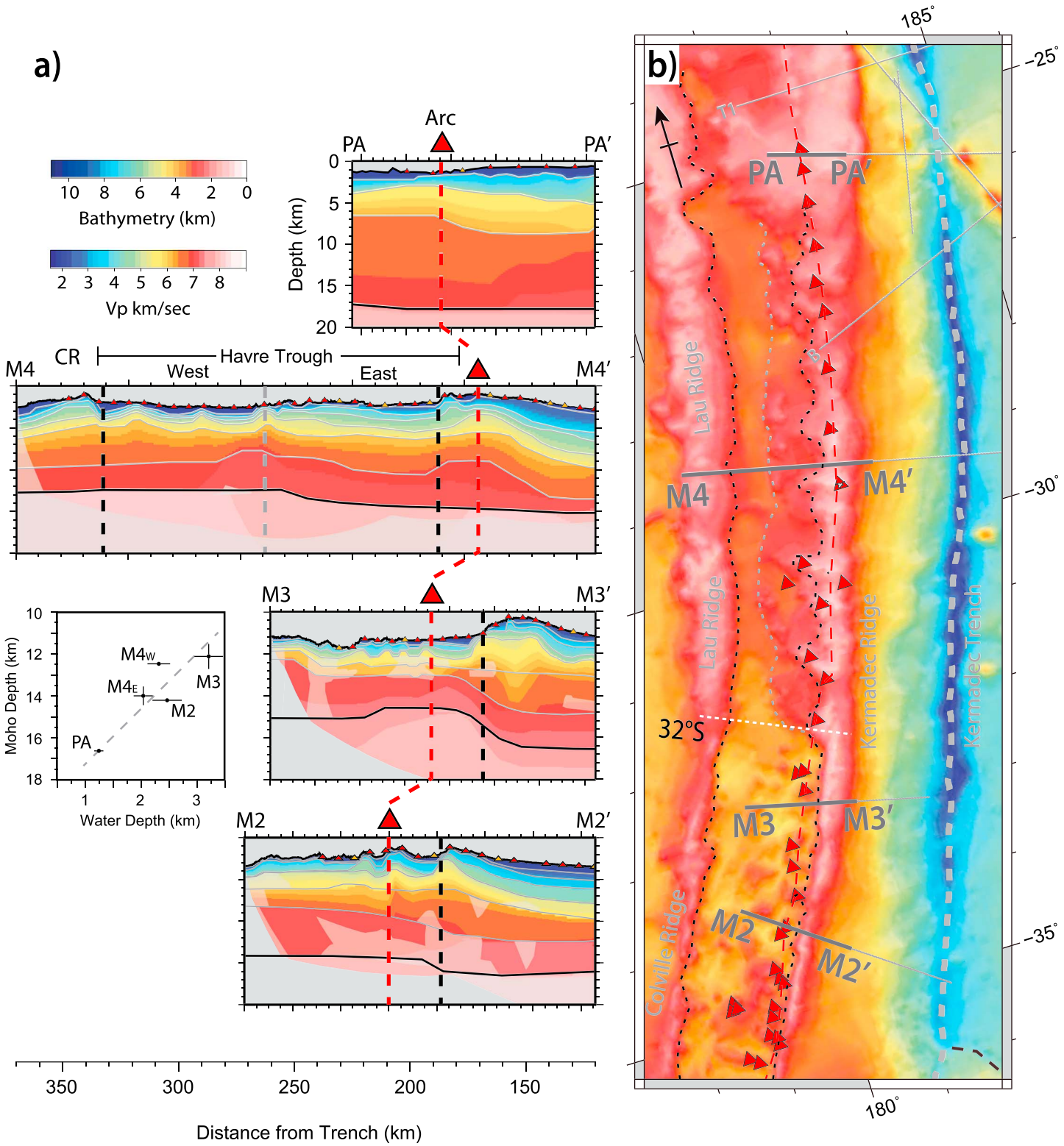

Figure 11. (a) Back-arc crustal structure and (b) bathymetry [*IOC et al.*, 2003] across the 32°S boundary (white dashed line from *Ballance et al.* [1999]). Seismic models are plotted against distance from the trench. Profile PA is from *Stratford et al.* [2015]. Black, grey, and red dashes mark the margins of the Havre Trough, our interpreted boundary between the western and eastern segments of the back-arc and the active volcanic arc, respectively. Note the contrast in Havre Trough water depth and the width of arc ridges across 32°S and the bathymetric contrast between the eastern and western segments of the northern Havre Trough [*Pelletier and Dupont*, 1990; *Wright*, 1997; *Ballance*, 1999].

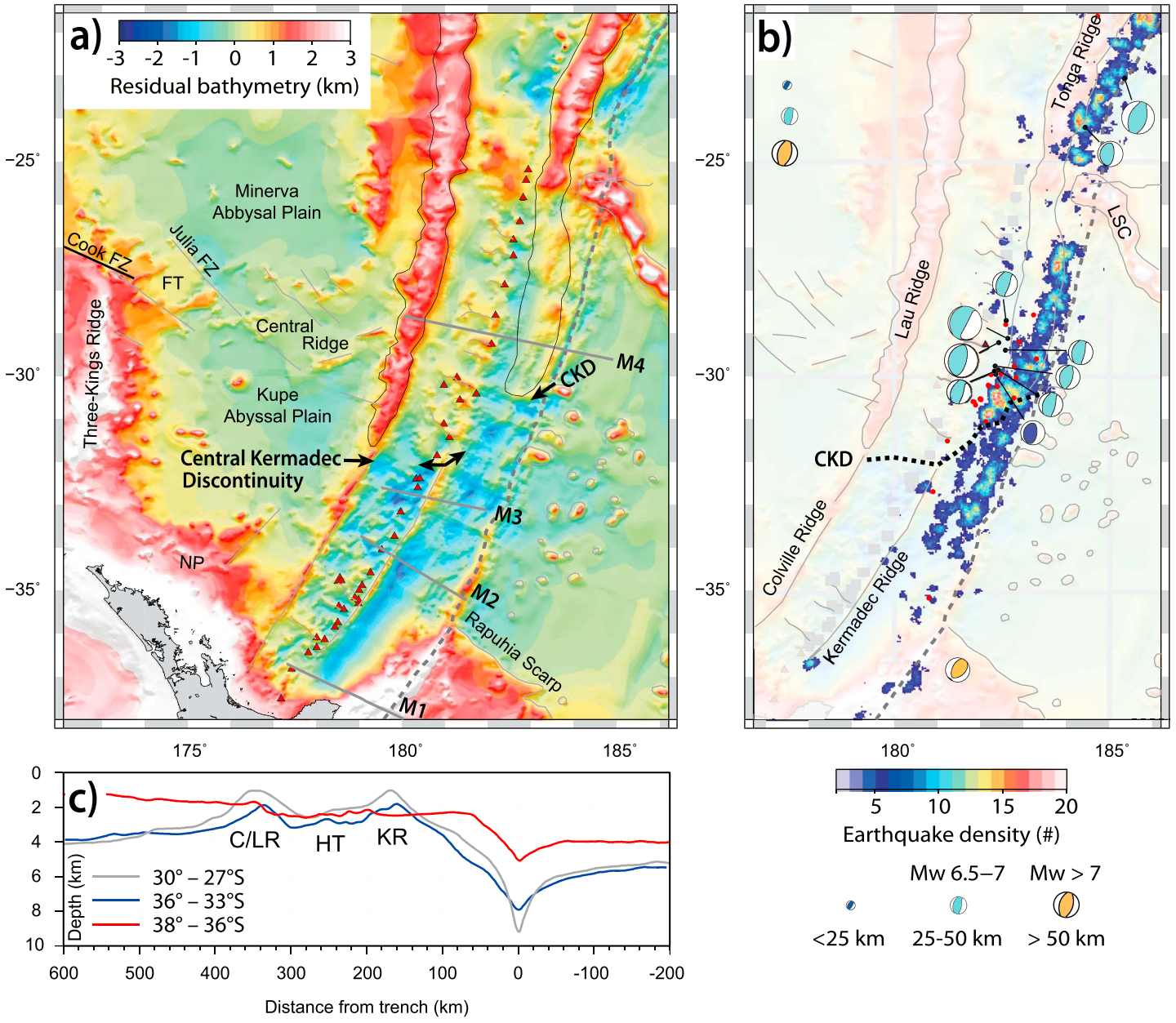

Figure 12. (a) Ensemble bathymetry. Thick grey dash marks the trench-axis. The Lau and Tonga Ridges are outlined in black, the latter of which is defined by the residual gravimetric expression shown in Figures 9 and 10. Our interpretation of the Central Kermadec Discontinuity (CKD) is shown by arrows in Figure 12a and dots Figure 12b. (b) EHB earthquake density calculated as the number of events (5 km search radius) in the EHB catalog with depth ≤ 60 km [*Engdahl et al.*, 1998]. Red dots show GCMT thrust earthquakes with $6.5 \leq M_w < 7.0$. Larger magnitude earthquakes are shown as focal mechanisms, which are scaled for magnitude and colored for depth [*Dziewonski et al.*, 1981; *Ekström et al.*, 2012]. Note the increase in the density and magnitude of earthquakes north of the CKD. (c) Ensemble average profiles calculated across the southern (red), central (blue), and northern (grey) Kermadec arc. Annotations are: NP = Northland Plateau; FT = Fantail Terrace; FZ = Fracture Zone; and LSC = Louisville Seamount Chain.

9. Residual Bathymetric Constraints on Upper Plate Structure and Relationships With Seismicity

The transition in back-arc morphology at 32°S was originally recognized as a transverse, ridge-perpendicular boundary across the Havre Trough and remnant arcs [*Pelletier and Dupont*, 1990]. The geometry of this transition may be an important discriminant between possible tectonic interpretations, and Figure 12a shows residual bathymetric anomalies calculated using the same spectral averaging technique applied to determine the latitudinal extent of the Tonga Ridge. In the Havre Trough, residual bathymetric anomalies illustrate a

W-E striking boundary at 32°S, which is similar to the original definition from *Pelletier and Dupont* [1990]. The easterly extension of this boundary through the fore-arc is also revealed, but in contrast to the back-arc segment, the fore-arc extension strikes SW-NE, intersecting the trench-axis at 30.5°S.

In the back-arc, this boundary is associated with a >1 km north-to-south increase in mean water depth in the Havre Trough and reductions in both the width (from >60 km to <30 km) and elevation (from ~1 km to ~1.7 km) of remnant arc ridges (Figures 2c and 12a). We interpret these abrupt and coincident reductions as marking the boundary between the Lau and Colville Ridges and estimate of the latitudinal extent of the Lau Ridge based on ridge width (>50 km) and the amplitude of residual bathymetric anomalies (amplitude >1.5 km). This definition suggests that the Lau Ridge terminates <50 km north of the bathymetric boundary. In the fore-arc, the southern limit of the residual gravimetric high shown to be associated with the Tonga Ridge (thin grey outline in Figure 12a) also terminates at the bathymetric boundary. The fore-arc divergence from 32°S requires the name of this boundary to be revised, and we propose the name "Central Kermadec Discontinuity" as the structural boundary between the northern and central segments of the Kermadec arc.

In the fore-arc, the Central Kermadec Discontinuity (CKD) (dotted black in Figure 12b) marks sharp north-to-south reductions in both the number and magnitude of earthquakes on the subduction megathrust and the gradient of the trench slope. Earthquake density is calculated as the number of events in the EHB catalog [*Engdahl et al*., 1998] with depth ≤60 km within a 5 km search radius. Between 29°S and 25°S, thrust earthquakes occur within 70 km of the trench-axis and only one event has $M_w \geq 6.5$. North but within ~100 km of the CKD, the density and magnitude of earthquakes increase significantly within a triangular region extending 110 km from the trench-axis containing 17 thrust earthquakes with $M_w \geq 6.5$ (Figure 12b). The southern boundary of this seismically active region correlates well with the CKD. South of this boundary, the contiguous band of earthquakes is restricted to trench distances ≤60 km and only two thrust earthquakes have $M_w \geq 6.5$ (Figure 12b).

The shallower outer fore-arc south of the Rapuhia scarp is associated with trench slope uplift above the subducting Hikurangi Plateau [*Collot and Davy*, 1998; *Davy and Collot*, 2000] and large residual bathymetric anomalies (amplitude >1.5 km) extend 90 km from the trench-axis (Figure 12a). Bathymetric anomalies associated with the Louisville Seamount Chain have similar amplitude but only extend 50 km from the trench-axis. In both regions, the landward extent of uplift is near the intersection of the subducting plate with the fore-arc Moho and the shallower trajectory of the subducting plate south of Rapuhia Scarp explains the variation in trench-slope uplift along strike (Figure 10b). These observations are consistent with global findings showing that trench-slope uplift associated with subducting relief is largest within 70 km of the trench-axis or landward of the slab-fore-arc-Moho intersection [*Bassett and Watts*, 2015a].

10. Discussion

Residual free-air gravity anomalies and the seismic velocity structure of the fore-arc (Figures 9 and 10) strongly support the suggestion of *Collot and Davy* [1998] that the Tonga Ridge occupies the Tonga-Kermadec fore-arc north of ~30.5°S. It is not known, however, whether this latitudinal extent is related to processes influencing the Paleogene formation and evolution of the Tonga Ridge or more recent Neogene subduction dynamics influencing its preservation. These hypotheses have contrasting predictions for the origin of the CKD, and each is considered below in the context of our new constraints on margin structure.

10.1. A Neogene Erosive Origin for the Central Kermadec Discontinuity

An erosional origin for the CKD has been proposed by *Collot and Davy* [1998] who suggest that the Tonga Ridge once extended along the length of the Kermadec trench, but has been eroded between 31°S and ~35°S by subduction of the Hikurangi Plateau. Assuming the western and northern margins of the Hikurangi Plateau were originally conjugate with the southern margins of the Ontong Java and Manihiki plateaus, respectively, *Reyners et al*. [2011] suggest the Hikurangi Plateau was a factor >2 larger than is presently observed at the surface and that at least half has been subducted in two episodes of subduction in the Cretaceous and Neogene. The reconstruction of *Chandler et al*. [2012] suggests an even larger extent for the Hikurangi Plateau which, when coupled with finite Pacific plate rotation poles relative to a fixed Australian plate [*Yan and Kroenke*, 1993; *Cande and Stock*, 2004], is shown by *Timm et al*. [2014] to have possibly resulted

in Hikurangi Plateau collision as far north as 33°S. *Timm et al*. [2014] suggest plateau subduction has accelerated the rate of tectonic erosion resulting in crustal thinning and subsidence of the upper plate.

Figure 12a shows that both the Lau and Tonga Ridges are similarly truncated by the CKD. This is a key observation as it implies the same truncation mechanisms for both ridges. Subducting relief in the form of seamounts, aseismic ridges, or LIPs provides one method of locally increasing rates of tectonic erosion, but these effects are typically focused near the trench-axis (within ~70 km) where quantities of uplift, fracturing, and subsequent trench-slope collapse are largest [*Ballance et al*., 1989; *Ranero and von Huene*, 2000; *Vannucchi et al*., 2013; *Bassett and Watts*, 2015a]. The width and geometry of the Tonga Ridge implies that the Lau Ridge was located at least 100 km arcward of the Tonga-Kermadec trench throughout the Neogene. We suggest this westerly offset makes it highly unlikely that the Lau Ridge has been eroded and truncated by subduction erosion. The only region where the Tonga Ridge may be experiencing significant basal tectonic erosion is between 26°S and 31°S where the ridge is nearer the trench-axis and potentially in contact with relief on the subducting slab.

10.2. Pre-Neogene Tectonic Inheritance for the Central Kermadec Discontinuity

West of the Tonga-Kermadec subduction zone is the South Fiji Basin [*Karig*, 1970], a 3–4 km deep back-arc basin bounded to the west by the Three Kings Ridge, Loyalty Ridge, and Cook Fracture Zone, to the east by Lau/Colville Ridge, and to the south by the Northland Plateau (Figure 12a). The basin is structurally subdivided by a rougher and shallower central ridge into the Minerva (north) and Kupe (south) Abyssal Plains [*Packham and Terrill*, 1976], and magnetic anomalies in both regions have been interpreted as recording Oligocene back-arc spreading [*Weissel and Watts*, 1975; *Watts et al*., 1977; *Davey*, 1982; *Malahoff et al*., 1982; *Sdrolias et al*., 2003]. Tectonic models for this region show major differences in the age of back-arc basins, the configuration of spreading centers and the number, age, and polarity of subduction zones [*A. J. Crawford et al*., 2003; *Sdrolias et al*., 2003; *Schellart et al*., 2006; *Mortimer et al*., 2007; *Herzer et al*., 2011]. Despite these differences, these models also display several important shared characteristics that suggest that the pre-Neogene evolution of the South Fiji Basin may have played a key role in generating the along-strike transitions in margin structure now observed in the Kermadec fore-arc and Havre Trough.

Island arc thoeleiites of Eocene age recovered from the eastern flank of the Tonga Ridge suggest that westward dipping subduction of the Pacific Plate along the Tonga-Kermadec arc began at circa 52–48 Ma [*Meffre et al*., 2012]. The oldest subduction-related lavas on the Norfolk and Three Kings Ridge have Oligocene ages (i.e., 32–26 Ma) [*Mortimer et al*., 2007], which suggests that subduction was initially focused along the northern Tonga arc [*A. J. Crawford et al*., 2003; *Meffre et al*., 2012]. In the late Eocene or early Oligocene, the Tonga trench began to rollback, which may have been accompanied by either minor clockwise [*A. J. Crawford et al*., 2003; *Schellart et al*., 2006; *Mortimer et al*., 2007; *Meffre et al*., 2012] or major anticlockwise [*Herzer et al*., 2011] rotation, depending on the original strike of the arc. Back-arc basin formation was restricted to the region north of the proto-Cook Fracture Zone [*A. J. Crawford et al*., 2003; *Meffre et al*., 2012]. In the early Oligocene, *A. J. Crawford et al*. [2003] and *Meffre et al*. [2012] show the Eocene arc—which hosts both the Tonga and Lau arc ridges—juxtaposed or connected with the Three Kings Ridge. *Mortimer et al*. [2007] and *Herzer et al*. [2011] show the same connection, albeit with the minor distinctions that they refer to this block as the Lau Terrace and suggest it was connected to the Three Kings Ridge via the Fantail Terrace (Figure 13a). In this manuscript we refer to this crustal fragment as the Eocene Arc substrate and its original continuity with the Three Kings Ridge is the first key observation supporting tectonic inheritance.

The offset of the Three Kings Ridge along the Cook Fracture Zones represents a fundamental post-arc structural discontinuity (Figure 13b). This offset occurred when the Minerva back-arc spreading center propagated through the Loyalty and Three Kings Ridges (and adjoining terraces), with back-arc spreading bifurcating east and west of the Three Kings Ridge into the Norfolk Basin and Kupe Abyssal Plain, respectively. It follows directly from the first key observation that some structure must have detached the Eocene Arc substrate from the Loyalty-Three Kings Ridge and accommodated its easterly translation as the Tonga-Kermadec trench rolled back. The recognition of these structures east of the Cook Fracture Zones is the second key observation supporting tectonic inheritance.

East of the Cook Fracture Zone, the South Fiji Basins Central Ridge is structurally complex and is characterized by a series of SW-NE striking bathymetric ridges/scarps (Figure 12a) and NW-SE striking lineaments in the

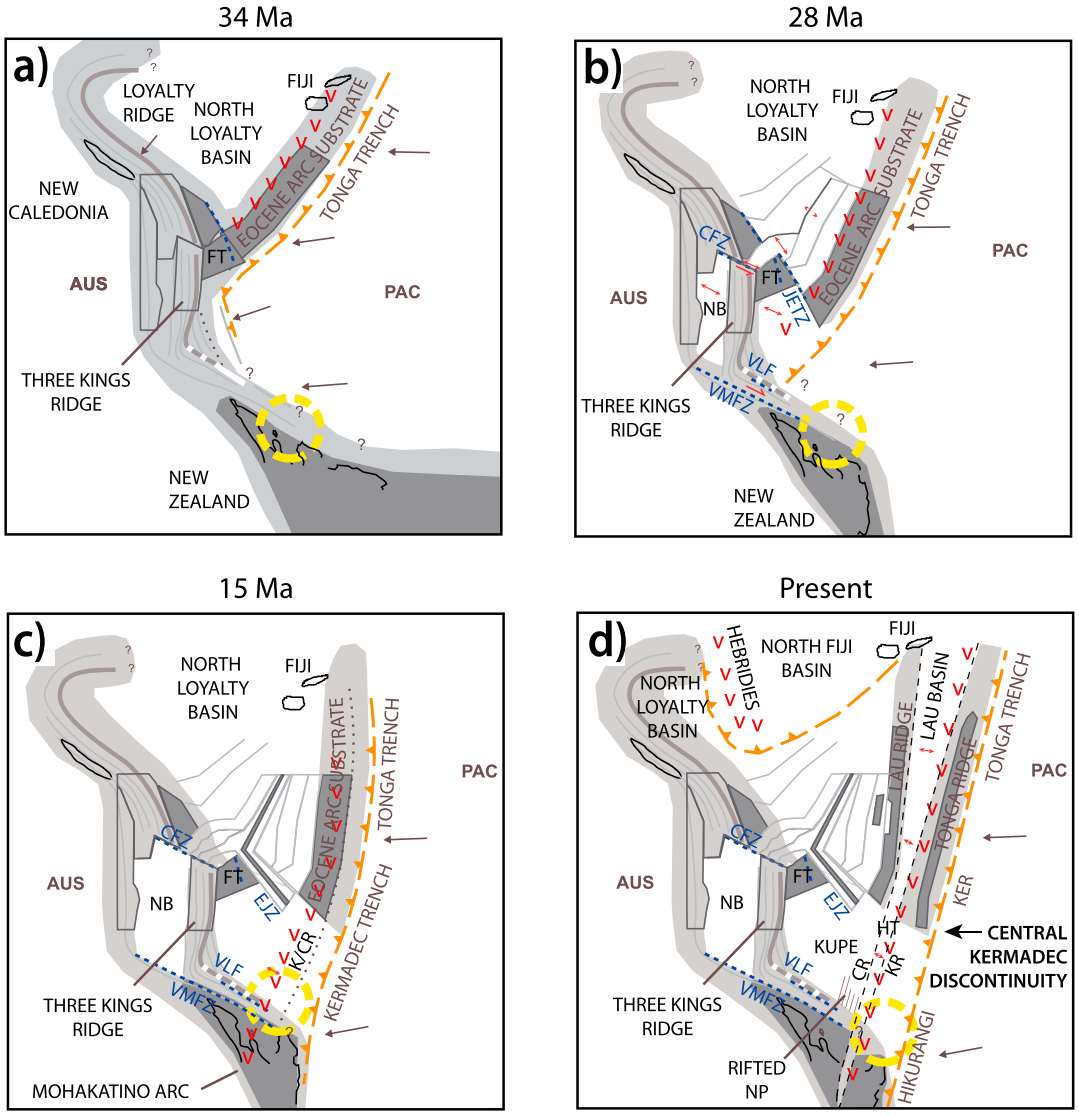

Figure 13. Panels illustrating the tectonic evolution of the South Fiji-Norfolk basin adapted from *Herzer et al.* [2011]. The Australian plate is fixed. Yellow dash marks Raukumara Basin. Transform margins/fracture zones are dashed in blue with subduction margins marked in orange. Red V's mark active volcanic arcs. Note that the crustal fragment labeled Eocene Arc Substrate was originally referred to as the Lau Terrace by *Herzer et al.* [2011]. Annotations are: FT = Fantail Terrace; CFZ = Cook Fracture Zone; JETZ = Julia Extensional Transform Zone; NB = Norfolk Basin; VLF = van der Linden Fault; VMFZ = Vening Meinesz Fracture Zone; K/CR = Kermadec/Colville Ridge; HT = Havre Trough; KUPE = Kupe Abyssal Plain; EJZ = East Julia Zone; AUS = Australian Plate; and PAC = Pacific Plate.

free-air gravity field (Figure 9a). Magnetic anomalies in the Minerva Abyssal Plain do not extend across this ridge [*Watts and Talwani*, 1974; *Weissel and Watts*, 1975; *Malahoff et al.*, 1982], so most tectonic models show this region separating the spreading centers of the Kupe and Minerva Abyssal Plains. *A. J. Crawford et al.* [2003] and *Sdrolias et al.* [2003] interpret the Julia Lineament (Julia FZ in Figure 12a) as a fossil spreading center associated with the southeasterly arm of the Minerva triple junction. *Sdrolias et al.* [2004] and *Schellart et al.* [2006], in contrast, show the Cook Fracture Zone (or a parallel equivalent) continuing across the South Fiji Basin, possibly extending to the Tonga-Kermadec trench. *Mortimer et al.* [2007] and *Herzer et al.* [2011] interpret the Fantail Terrace as extended arc crust and suggest that rifting of this block and transform motion along the Julia Lineament accommodated the detachment and easterly translation of the Eocene Arc substrate away from the Three Kings Ridge in the early Oligocene.

The latter model incorporates chronological and petrological constraints from *Mortimer et al*. [2007] and *Mortimer et al*. [2010] and is more consistent with the SW-NE trend of rifted fault blocks north and east of the Three Kings Ridge and seismic and swath bathymetry data [*Davey*, 1982; *Herzer et al*., 2011] associating the Julia Lineament with a transform fault scarp. Gravity lineations in the South Fiji Basin (Figure 9) also appear to map the southern tip of the Eocene Arc substrate back to the rifted Fantail Terrace, suggesting an association with fracture zones. A simplified version of the *Herzer et al*. [2011] reconstruction is shown in Figure 13. The implication of the first shared observation is that the Eocene Arc substrate, and hence the Tonga and Lau Ridges, did not extend the length of the Tonga-Kermadec trench (Figure 13a). The implication of the second shared observation is that the southern extent of the Eocene Arc substrate, and hence the Central Kermadec Discontinuity (CKD), was likely formed during separation from the Fantail Terrace (or Three Kings Ridge) and was possibly coeval with the Cook Fracture Zone (Figures 13b–13d).

10.3. Implications for Along-Strike Variations in Crustal Structure

Figure 14a shows Bouguer gravity anomalies calculated from satellite derived free-air gravity grids [*Sandwell and Smith*, 2009] assuming densities $\rho_{water} = 1030\ kg\ m^{-3}$ and $\rho_{crust} = 2700\ kg\ m^{-3}$. From this grid, we recognize three main structural elements. These are (a) the Eocene Arc substrate, hosting the Lau and Tonga Ridges; (b) the Kupe Abyssal Plain; and (c) the relict Gondwana margin, which is best preserved and relatively undeformed in Raukumara Basin. It is important to note that margin-normal transitions in Bouguer gravity anomalies between these domains appear continuous between the fore-arc, Havre Trough, and the region west of the Lau/Colville Ridge (Figure 14a).

South of ~35°S, Raukumara Basin preserves Cretaceous and Paleogene strata and the Mesozoic Gondwana trench slope is tentatively interpreted beneath the western margin of the basin [*Sutherland et al*., 2009]. Gondwana fore-arc rocks are widely observed onshore on both the Raukumara (Jurassic and Cretaceous Torlesse Supergroup) and Northland (Permo-Triassic Waipapa greywacke) Peninsulas [*Mazengarb and Speden*, 2000; *Mortimer*, 2004]. Allochthonous sheets were emplaced on both peninsulas in the latest Oligocene-earliest Miocene [*Stoneley*, 1968; *Rait et al*., 1991; *Mazengarb and Speden*, 2000] and a correlative allochthon is observed offshore [*Sutherland et al*., 2009]. Raukumara Basin is suggested to preserve an old Cretaceous trench and was effectively an ocean-continent transition [*Sutherland et al*., 2009]. The crust underlying the central basin has normal oceanic thickness (~6–7 km) [*Sutherland et al*., 2009; *Bassett et al*., 2010; *Scherwath et al*., 2010], the age of which must at least predate the cessation of Gondwana deformation and volcanism onshore (85–105 Ma) [*Mazengarb and Speden*, 2000]. The similarities described above and the continuity in Bouguer gravity anomalies between the fore-arc and back-arc leads us to suggest that the intervening arc most likely formed on crust of similar Mesozoic age and Gondwana margin origin.

North of the CKD, the overthrusting plate is comprised of the Eocene Arc substrate and associated ridges. Subduction beneath this substrate has been ongoing since the early Eocene and the Tonga fore-arc preserves the Eocene subduction initiation sequence [*Meffre et al*., 2012]. The ages of Eocene fore-arc basalts (FABs) and related gabbros are similar along the Tonga (52–49 Ma), Izu Bonin (51–52 Ma) [*Ishizuka et al*., 2011], and Mariana (51.5 ± 0.7 Ma) [*Reagan et al*., 2013] arcs, linking subduction initiation along the western Pacific. The oldest rocks recovered from the Tonga fore-arc are mid-Cretaceous FABs [*Meffre et al*., 2012]. The geochemistry of these rocks is unlike the Pacific Plate Mid-Ocean Ridge Basalts (MORBs) and the similarity in age with detrital-zircon populations and associated volcanics in New Caledonia and New Zealand led *Falloon et al*. [2014] to suggest that the basement of the Tonga fore-arc may have formed in a Cretaceous back-arc basin. This is similar to the interpretation of Mesozoic (159.4 ± 0.8 Ma) FABs recovered beneath gabbroic layers in the Izu Bonin-Mariana (IBM) system [*Ishizuka et al*., 2011]. Similar to the Raukumara segment of the fore-arc, it is possible the northern Kermadec arc is also composed of Mesozoic basement and younger (Eocene to present) subduction-related rocks.

The central Kermadec arc is characterized by the largest Bouguer gravity anomalies (Figure 14) [*Timm et al*., 2014] and the region of thinnest crust (8–9 km) in the Havre Trough (Figure 11). In contrast to the northern (Eocene arc substrate) and southern (Gondwana) segments of the arc, the age and provenance of the central Kermadec arc is poorly constrained by rock samples. Hence, the key information is the tectonic interpretation of the segment margins. We suggest that the northern boundary (labeled 1 in Figure 14) is

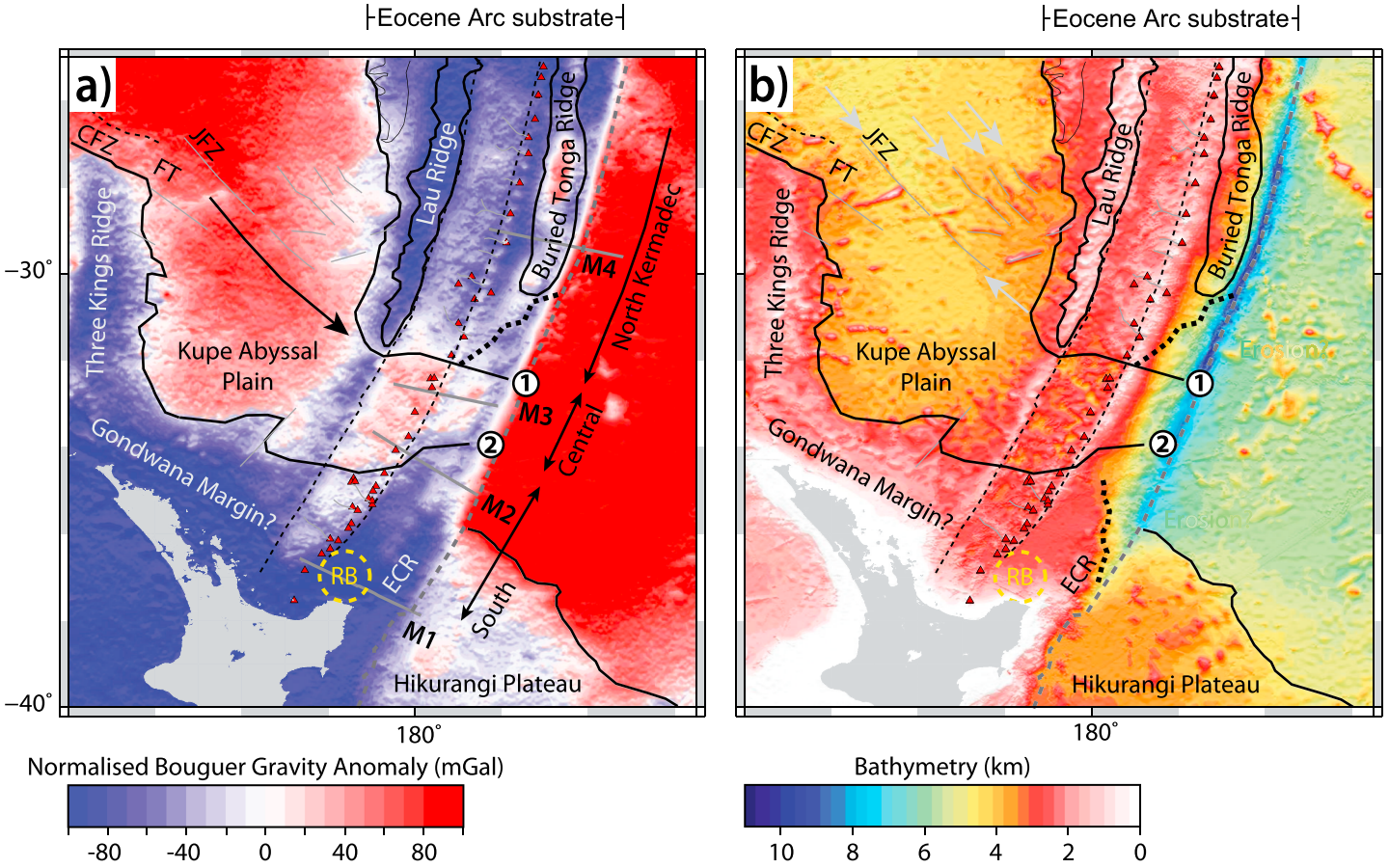

Figure 14. Summary of structural domains interpreted from the tectonic reconstruction in Figure 13 shown against (a) Bouguer gravity anomalies and (b) bathymetry. Note the continuity in Bouguer gravity anomalies across the fore-arc, arc, and back-arc. We suggest the north Kermadec arc has been constructed on a substrate of the Eocene arc, the central Kermadec arc on rifted arc crust, and the southern Kermadec arc on the relict Gondwana margin. Labels 1 and 2 mark the southern boundary of the Lau Terrace and the northern boundary of the relict Gondwana margin, respectively. Annotations are: RB = Raukumara Basin; ECR = East Cape Ridge; CFZ = Cook Fracture Zone; FT = Fantail Terrace; and JFZ = Julia Fracture Zone.

clearly associated with the rifted southern boundary of the Eocene arc substrate. The southern boundary (labeled 2 in Figure 14) is diffuse but appears continuous with the back-arc transition between the Gondwana margin and the Kupe Abyssal Plain. The basement of the central Kermadec arc may thus have formed in the Kupe Abyssal Plain.

This interpretation predicts that the central Kermadec arc should not contain either Mesozoic basement or Eocene arc rocks and provides an alternative explanation for the anomalous water depth and reduced crustal thickness of the Havre Trough back-arc [*Collot and Davy*, 1998; *Timm et al*., 2014]. Magnetic lineations in the Kupe Abyssal Plain are complex and suggest basin formation at an east-northeast migrating triple junction [*Sutherland*, 1999; *Sdrolias et al*., 2003]. This interpretation is contrary to earlier interpretations of magnetic anomalies younging west rather than east [*Davey*, 1982; *Malahoff et al*., 1982] but is more consistent with the rifted eastern margin of the Three Kings Ridge [*Herzer et al*., 2009]. The southern arm of this triple junction is interpreted to strike approximately N-S at a longitude of ~177°E [*Sutherland*, 1999; *Sdrolias et al*., 2003]. Pure arc-perpendicular extension would form magnetic lineations extending parallel (N-S) to the spreading arm, but magnetic lineations east of this spreading arm are oblique, striking NW-SE. These NW striking lineations align with the East Julia Zone and earlier interpretations of NW striking magnetic lineations in the southern Minerva Abyssal Plain [*Davey*, 1982].

Magnetic and structural fabrics are not everywhere arc parallel and all previous interpretations involve at least one ridge-ridge-ridge triple junction [*Weissel and Watts*, 1975; *Watts et al*., 1977; *Davey*, 1982; *Sutherland*, 1999; *A. J. Crawford et al*., 2003; *Sdrolias et al*., 2003; *Mortimer et al*., 2007; *Herzer et al*., 2011].

This back-arc configuration requires that the arc change shape. Arc lengthening will occur in most scenarios and is required if it is intersected by magnetic lineations (and not spreading obliquely). Near and south of the East Julia Zone, magnetic lineations strike NW and are highly oblique to the Lau-Colville Ridge. We suggest this obliquity requires some component of arc-parallel extension in the back-arc and likely occurred during the interval 28–20 Ma (Figure 13) based on ties to Deep Sea Drilling Project (DSDP) Site 205 [*Davey*, 1982]. Arc-parallel extension has been similarly interpreted in the North Fiji Basin where magnetic anomalies and spreading ridges strike at high angles to the strike of the New Hebridies arc [*Pelletier et al*., 1993; *Schellart et al*., 2002, 2006].

We suggest this arc-parallel extension (thinning) in addition to arc-perpendicular extension (splitting) may have played a role in reducing the inherited crustal thickness of the central Kermadec arc. The effect may be small and inheritance may be much more significant, but some component of arc-parallel extension is required by the oblique geometry of magnetic lineations. Oblique rifting in the Havre Trough since the Pliocene provides further evidence of margin parallel strains being accommodated in the back-arc. Rift fabric is more oblique (29–38°) to the basin axis north of the CKD (26°S–31°S) than in the back-arc of the central Kermadec arc (13–20° between 32°S and 34°S) and the approximately constant width of the Havre Trough (179 ± 30 km) suggests similar degrees of extension perpendicular to strike [*Delteil et al*., 2002].

Along-strike variations in Kermadec arc crustal structure can thus be explained by (a) inheritance from pre-Neogene tectonics, (b) extension perpendicular *and* parallel to strike, and (c) subduction erosion and lower crustal underplating. We suggest that first-order margin parallel transitions are likely inherited from before the Neogene and reflect Mesozoic crustal structure and along-strike variations in the duration of arc volcanism. The oldest arc related rocks north and south of the CKD are ~52 Ma (Tonga Ridge) [*Meffre et al*., 2012] and 16.7 Ma (Colville Ridge) [*Mortimer et al*., 2010], respectively, and the contrast in the duration of arc volcanism is expressed in the dimensions of arc ridges. The CKD formed during the Oligocene separation of the Eocene arc from the Three Kings Ridge and arc-parallel extension in the Kupe Abyssal Plain may have played a role in reducing the inherited crustal thickness of the central Kermadec arc. These fundamental, along arc transitions have been subsequently modified in the back-arc by spreading in the Havre Trough [*Delteil et al*., 2002]. In the fore-arc, subduction erosion associated with oceanic plateau subduction provides a viable explanation for the incised morphology of the outer fore-arc between 31°S and ~35°S [*Collot and Davy*, 1998; *Timm et al*., 2014], and plateau subduction and lower crustal underplating are currently driving uplift at the East Cape Ridge. While each of the factors described above have clearly influenced the structure of the Kermadec arc, we suggest that pre-Neogene tectonic inheritance is possibly the most significant and has not previously been identified as such.

11. Summary and Conclusions

We have analyzed three wide-angle seismic refraction profiles and applied spectral averaging techniques to regional grids of bathymetry and free-air gravity anomaly to place the first regional constraints on the structure of the Kermadec arc.

The northern Kermadec fore-arc (32°S–25°S) is occupied by the extinct Eocene Tonga Ridge arc. This ridge has V_P 6.5–7.3 km s^{-1} and residual gravity anomalies constrain its latitudinal extent (18.5°S to 30.5°S) width (110 ± 20 km) and strike (~005° south of 25°S). Fore-arc Moho depth is 15 ± 2 km and the mantle wedge has V_P 7.8–8.1 km s^{-1}. Crustal thickness in the northern Havre Trough (25°S to 32°S) is up to 12 km thick and is structurally segmented into east and west domains of equal width. Basins and fault blocks associated with Plio-Pleistocene rifting between the Lau and Tonga ridges are preserved in the deeper western Havre Trough, but have been overprinted by recent volcanism in the thicker and shallower eastern region. The crust of the subducting Pacific plate is 6 ± 1 km thick, has V_P 6.0–7.2 km s^{-1}, and increases in dip from 8–9° to 17–18° at ~19 km depth.

The Central Kermadec fore-arc (~34°S–32°S) is structurally homogeneous downdip with V_P 5.7–7.3 km s^{-1}. Lower crustal velocities are similar to the northern Kermadec fore-arc but there is no seismic or gravimetric evidence for an extinct arc ridge within the fore-arc. The fore-arc Moho is planar at 16 km depth and the mantle wedge has V_P 7.7–7.9 km s^{-1}. Crustal thickness in the central Havre Trough is 8–9 km, which is up to 4 km

thinner than the western Havre Trough equidistant from the trench but north of the Central Kermadec Discontinuity, and at least 1 km thinner than the southern Havre Trough.

The Southern Kermadec fore-arc (~34°S–~37°S) is characterized by a central 4.5 km deep fore-arc basin bounded by fore-arc ridges. The thickness of crust underlying the central basin (6–7 km) is comparable to Raukumara Basin imaged farther south [*Sutherland et al*., 2009; *Bassett et al*., 2010; *Scherwath et al*., 2010]. The ridge bounding the basin to the east is also gravimetrically contiguous with the East Cape Ridge, and these structures may be linked along strike. Fore-arc Moho depth is 16 km and V_P in the mantle wedge is ~8.1 km s^{-1}.

We infer that the northern Kermadec and Tonga arc comprise a substrate of the Eocene arc. This substrate preserves the Eocene subduction initiation sequence, has been a site of arc volcanism since the early Eocene and may be floored by Mesozoic crust [*Meffre et al*., 2012; *Falloon et al*., 2014]. Plate tectonic reconstructions show that the Eocene volcanic arc was originally conjoined with the Three Kings Ridge or Fantail terrace [*A. J. Crawford et al*., 2003; *Schellart et al*., 2006; *Mortimer et al*., 2007; *Herzer et al*., 2011] but was detached during the early Oligocene and translated east to its current position as the Tonga trench rolled back. We suggest this separation formed the Central Kermadec Discontinuity (previously known as the 32°S boundary) and we constrain the geometry of this discontinuity in the fore-arc and back-arc using residual bathymetric anomalies.

The southern Kermadec fore-arc also preserves Mesozoic rocks accreted at the relic Gondwana margin [*Sutherland et al*., 2009]. We suggest that the Raukumara block may be >350 km long extending as far north as 34°S and that the northern boundary of this block may be analogous to the back-arc transition between the Northland region of New Zealand and the Kupe Abyssal Plain. This interpretation implies that crust in the central Kermadec arc may have formed in the Kupe Abyssal Plain. Magnetic lineations in this region are oblique to the N-S spreading center [*Sutherland et al*., 2009], and margin parallel extension may have played a role in reducing the inherited crustal thickness in the central Kermadec arc. In contrast to the Eocene arc farther north [*Meffre et al*., 2012], the oldest rocks dredged from the central and southern Kermadec arcs have Middle Miocene ages [*Mortimer et al*., 2010] and the smaller dimensions of the Kermadec and Colville ridges are consistent with the factor >2 reduction in the duration of arc volcanism.

Along-strike variations in Kermadec arc crustal structure can be explained by (a) inheritance from pre-Neogene tectonics, (b) extension perpendicular and parallel to strike, and (c) subduction erosion and lower crustal underplating. Although they have all played a role, we suggest pre-Neogene inheritance was the most significant and provides the most viable mechanism of generating the first-order along-strike transitions in margin structure observed in this study.

Acknowledgments

We thank Captain Mallon and the officers and crew of the R/V *SONNE*. We thank Paul Tregoning, the Associate Editor, Nick Mortimer, and J. Kim Welford for their reviews that helped improve the manuscript. Shamita Das, Jason Phipps Morgan, and Jake Perez are thanked for their helpful comments on an early version of this manuscript. Wanda Stratford is thanked for providing her seismic velocity model along SO215 Profile A (PA). Seismic processing was conducted using GLOBE Claritas and Guy Maslen is thanked for support provided. Figures were constructed using the Generic Mapping Tools [*Wessel and Smith*, 1991, 1995, 1998]. D.B. was supported by a University of Oxford Clarendon Scholarship, by a Green Foundation Postdoctoral Fellowship in the Institute of Geophysics and Planetary Physics, Scripps Institution of Oceanography, University of California, San Diego, by the National Geospatial Agency (HM01771310008), and by the Scripps Seafloor Electromagnetics Consortium (http://marineemlab.ucsd.edu/semc.html). The data analyzed in this study will be made available on request (dbassett@ucsd.edu).

References

Austin, J. A., F. W. Taylor, and C. D. Cagle (1989), Seismic stratigraphy of the central Tonga Ridge, *Mar. Pet. Geol.*, *6*, 71–92.

Ballance, P. F. (1999), Simplification of the Southwest Pacific Neogene arcs: Inherited complexity and control by a retreating pole of rotation, *Geol. Soc. Spec. Publ.*, *164*, 7–19.

Ballance, P. F., D. W. Scholl, T. L. Vallier, and R. H. Herzer (1989), Subduction of a Late Cretaceous seamount of the Louisville Ridge at the Tonga Trench: A model of normal and accelerated tectonic erosion, *Tectonics*, *8*, 953–962, doi:10.1029/TC008i005p00953.

Ballance, P. F., A. G. Ablaev, I. K. Pushchin, S. P. Pletnev, M. G. Birylina, T. Itaya, H. A. Follas, and G. W. Gibson (1999), Morphology and history of the Kermadec Trench-arc-backarc basin-remnant arc system at 30 to 32 degrees S: Geophysical profile, microfossil and K-Ar data, *Mar. Geol.*, *159*(1-4), 35–62.

Bassett, D., and A. B. Watts (2015a), Gravity anomalies, crustal structure, and seismicity at subduction zones: 1. Seafloor roughness and subducting relief, *Geochem. Geophys. Geosyst.*, *16*, 1508–1540, doi:10.1002/2014GC005684.

Bassett, D., and A. B. Watts (2015b), Gravity anomalies, crustal structure, and seismicity at subduction zones: 2. Interrelationships between fore-arc structure and seismogenic behavior, *Geochem. Geophys. Geosyst.*, *16*, 1541–1576, doi:10.1002/2014GC005685.

Bassett, D., R. Sutherland, S. Henrys, T. Stern, M. Scherwath, A. Benson, S. Toulmin, and M. Henderson (2010), Three-dimensional velocity structure of the northern Hikurangi margin, Raukumara, New Zealand: Implications for the growth of continental crust by subduction erosion and tectonic underplating, *Geochem. Geophys. Geosyst.*, *11*, Q10013, doi:10.1029/2010GC003137.

Bassett, D., D. T. Sandwell, Y. Fialko, and A. B. Watts (2016), Upper-plate controls on co-seismic slip in the 2011 Magnitude 9.0 Tohoku-oki earthquake, *Nature*, doi:10.1038/nature16945.

Bevis, M., et al. (1995), Geodetic observations of very rapid convergence and back-arc extension at the Tonga Arc, *Nature (London)*, *374*(6519), 249–251.

Billen, M. I., and M. Gurnis (2001), A low viscosity wedge in subduction zones, *Earth Planet. Sci. Lett.*, *193*(1), 227–236.

Billen, M. I., M. Gurnis, and M. Simons (2003), Multiscale dynamics of the Tonga-Kermadec subduction zone, *Geophys. J. Int.*, *153*, 359–388.

Bott, M. (1965), The deep sructure of the Northern Irish Sea-a problem of crustal dynamics, in *Submarine Geology and Geophysics*, edited by W. F. Whittard and R. Bradshaw, *Colston Pap.*, vol. 17, pp. 179–204 Butterworth, London.

Brocher, T. M. (2005), Empirical relations between elastic wavespeeds and density in the Earth's crust, *Bull. Seismol. Soc. Am.*, *95*(6), 2081–2092.

Buiter, S. J., R. Govers, and M. Wortel (2001), A modelling study of vertical surface displacements at convergent plate margins, *Geophys. J. Int.*, *147*(2), 415–427.
Cande, S. C., and J. M. Stock (2004), Pacific-Antarctic-Australia motion and the formation of the Macquarie Plate, *Geophys. J. Int.*, *157*, 399–414.
Carlson, R. L., and D. J. Miller (2003), Mantle wedge water contents estimated from seismic velocities in partially serpentinized peridotites, *Geophys. Res. Lett.*, *30*(5), 1250, doi:10.1029/2002GL016600.
Chandler, M. T., P. Wessel, B. Taylor, M. Seton, S.-S. Kim, and K. Hyeong (2012), Reconstructing Ontong Java Nui: Implications for Pacific absolute plate motion, hotspot drift and true polar wander, *Earth Planet. Sci. Lett.*, *331*, 140–151.
Christensen, N. I. (1966), Elasticity of ultrabasic rocks, *J. Geophys. Res.*, *71*, 5921–5931, doi:10.1029/JZ071i024p05921.
Christensen, N. I. (1996), Poisson's ratio and crustal seismology, *J. Geophys. Res.*, *101*, 3139–3156, doi:10.1029/95JB03446.
Clift, P. D. (1994), Sedimentation on the Tonga forearc related to arc rifting, subduction erosion, and ridge collision: A synthesis of results from Sites 840 and 841, in *Proceedings of the Ocean Drilling Program, Sci. Results, Lau Basin*, vol. 135, pp. 843–855, Ocean Drill. Program, College Station, Tex.
Clift, P. D., and C. J. MacLeod (1999), Slow rates of subduction erosion estimated from subsidence and tilting of the Tonga forearc, *Geology*, *27*(5), 411–414.
Collot, J. Y., and B. Davy (1998), Forearc structures and tectonic regimes at the oblique subduction zone between the Hikurangi Plateau and the southern Kermadec margin, *J. Geophys. Res.*, *103*, 623–650, doi:10.1029/97JB02474.
Contreras-Reyes, E., I. Grevemeyer, A. B. Watts, E. R. Flueh, C. Peirce, S. Moeller, and C. Papenberg (2011), Deep seismic structure of the Tonga subduction zone: Implications for mantle hydration, tectonic erosion, and arc magmatism, *J. Geophys. Res.*, *116*, B10103, doi:10.1029/2011JB008434.
Crawford, A. J., S. Meffre, and P. Symonds (2003), 120 to 0 Ma tectonic evolution of the southwest Pacific and analogous geological evolution of the 600 to 220 Ma Tasman Fold Belt System, *Geol. Soc. Aust. Spec. Publ.*, *22*, 377–397.
Crawford, W. C., J. A. Hildebrand, L. M. Dorman, S. C. Webb, and D. A. Wiens (2003), Tonga Ridge and Lau Basin crustal structure from seismic refraction data, *J. Geophys. Res.*, *108*(B4), 2195, doi:10.1029/2001JB001435.
Davey, F. J. (1982), The structure of the South Fiji Basin, *Tectonophysics*, *87*(1-4), 185–241.
Davies, G. F. (1981), Regional compensation of subducted lithosphere: Effects on geoid, gravity and topography from a preliminary model, *Earth Planet. Sci. Lett.*, *54*(3), 431–441.
Davy, B., and J.-Y. Collot (2000), The Rapuhia Scarp (northern Hikurangi Plateau): Its nature and subduction effects on the Kermadec Trench, *Tectonophysics*, *328*, 269–295.
Davy, B., and R. Wood (1994), Gravity and magnetic modelling of the Hikurangi Plateau, *Mar. Geol.*, *118*, 139–151.
Davy, B., K. Hoernle, and R. Werner (2008), Hikurangi Plateau: Crustal structure, rifted formation, and Gondwana subduction history, *Geochem. Geophys. Geosyst.*, *9*, Q07004, doi:10.1029/2007GC001855.
DeBari, S., and A. Greene (2011), Vertical stratification of composition, density, and inferred magmatic processes in exposed arc crustal sections, in *Arc-Continent Collision*, *Fontiers in Earth Science*, pp. 121–144, Springer, Berlin.
Delteil, J., E. Ruellan, I. Wright, and T. Matsumoto (2002), Structure and structural development of the Havre Trough (SW Pacific), *J. Geophys. Res.*, *107*(B7), 2143, doi:10.1029/2001JB000494.
DeMets, C., R. G. Gordon, D. F. Argus, and S. Stein (1994), Effect of recent revisions to the geomagnetic time scale on estimates of current plate motions, *Geophys. Res. Lett.*, *21*, 2191–2194, doi:10.1029/94GL02118.
DeMets, C., R. G. Gordon, and D. F. Argus (2010), Geologically current plate motions, *Geophys. J. Int.*, *181*(1), 1–80, doi:10.1111/j.1365-246X.2009.04491.x.
de Ronde, C., et al. (2007), Submarine hydrothermal activity along the mid-Kermadec Arc, New Zealand: Large-scale effects on venting, *Geochem. Geophys. Geosyst.*, *8*, Q07007, doi:10.1029/2006GC001495.
de Ronde, C. E., E. T. Baker, G. J. Massoth, J. E. Lupton, I. C. Wright, R. A. Feely, and R. R. Greene (2001), Intra-oceanic subduction-related hydrothermal venting, Kermadec volcanic arc, New Zealand, *Earth Planet. Sci. Lett.*, *193*(3), 359–369.
de Ronde, C. E., G. Massoth, E. T. Baker, J. E. Lupton, S. Simmons, and I. Graham (2003), Submarine hydrothermal venting related to volcanic arcs, in *Volcanic, Geothermal and Ore-Forming Fluids: Rulers and Witnesses of Processes Within the Earth*, *Soc. Econ. Geol. Spec. Publ., 10*, Johnson Printing, Boulder, Colo.
Dziewonski, A., T. A. Chou, and J. Woodhouse (1981), Determination of earthquake source parameters from waveform data for studies of global and regional seismicity, *J. Geophys. Res.*, *86*, 2825–2852, doi:10.1029/JB086iB04p02825.
Ekström, G., M. Nettles, and A. Dziewoński (2012), The global CMT project 2004–2010: Centroid-moment tensors for 13,017 earthquakes, *Phys. Earth Planet. Inter.*, *200*, 1–9.
Engdahl, E. R., R. van der Hilst, and R. Buland (1998), Global teleseismic earthquake relocation with improved travel times and procedures for depth determination, *Bull. Seismol. Soc. Am.*, *88*(3), 722–743.
Falloon, T. J., S. Meffre, A. J. Crawford, K. Hoernle, F. Hauff, S. H. Bloomer, and D. J. Wright (2014), Cretaceous fore-arc basalts from the Tonga arc: Geochemistry and implications for the tectonic history of the SW Pacific, *Tectonophysics*, *630*, 21–32.
Flueh, E. R., and H. Kopp (2007), *FS Sonne Fahrtbericht/Cruise Report SO 192-1 MANGO: Marine Geoscientific Investigations on the Input and Output of the Kermadec Subduction Zone; Auckland-Auckland, 24.03.-22.04.2007*, IFM-GEOMAR Kiel, Germany.
Gamble, J., and I. Wright (1995), The southern Havre Trough geological structure and magma petrogenesis of an active backarc rift complex, in *Backarc Basins*, edited by B. Taylor, pp. 29–62, Plenum Press, New York.
Haase, K. M., T. J. Worthington, P. Stoffers, D. Garbe-Schönberg, and I. Wright (2002), Mantle dynamics, element recycling, and magma genesis beneath the Kermadec Arc-Havre Trough, *Geochem. Geophys. Geosyst.*, *3*(11), 1071, doi:10.1029/2002GC000335.
Hayes, G. P., and D. J. Wald (2009), Developing framework to constrain the geometry of the seismic rupture plane on subduction interfaces a priori—A probabilistic approach, *Geophys. J. Int.*, *176*(3), 951–964.
Hayes, G. P., D. J. Wald, and R. L. Johnson (2012), Slab1.0: A three-dimensional model of global subduction zone geometries, *J. Geophys. Res.*, *117*, B01302, doi:10.1029/2011JB008524.
Henrys, S., M. Reyners, I. Pecher, S. Bannister, Y. Nishimura, and G. Maslen (2006), Kinking of the subducting slab by escalator normal faulting beneath the North Island of New Zealand, *Geology*, *34*(9), 777–780.
Herzer, R. H., B. Davy, N. Mortimer, P. G. Quilty, G. C. H. Chaproniere, C. M. Jones, A. J. Crawford, and C. J. Hollis (2009), Seismic stratigraphy and structure of the Northland Plateau and the development of the Vening Meinesz transform margin, SW Pacific Ocean, *Mar. Geophys. Res.*, *30*(1), 21–60, doi:10.1007/s11001-009-9065-1.
Herzer, R. H., D. Barker, W. Roest, and N. Mortimer (2011), Oligocene-Miocene spreading history of the northern South Fiji Basin and implications for the evolution of the New Zealand plate boundary, *Geochem. Geophys. Geosyst.*, *12*, Q02004, doi:10.1029/2010GC003291.
Hyndman, R., and S. Peacock (2003), Serpentinization of the forearc mantle, *Earth Planet. Sci. Lett.*, *212*(3), 417–432.

Intergovernmental Oceanographic Commission (IOC), IHO, and BODC (2003), Centenary Edition of the GEBCO Digital Atlas [CD-ROM], published on behalf of the Intergovernmental Oceanographic Commission and the International Hydrographic Organization as part of the General Bathymetric Chart of the Oceans, Br. Oceanogr. Data Cent., Liverpool.

Isacks, B., J. Oliver, and L. R. Sykes (1968), Seismology and the new global tectonics, *J. Geophys. Res.*, *73*, 5855–5899, doi:10.1029/JB073i018p05855.

Ishizuka, O., K. Tani, M. K. Reagan, K. Kanayama, S. Umino, Y. Harigane, I. Sakamoto, Y. Miyajima, M. Yuasa, and D. J. Dunkley (2011), The timescales of subduction initiation and subsequent evolution of an oceanic island arc, *Earth Planet. Sci. Lett.*, *306*(3), 229–240.

Karig, D. E. (1970), Ridges and basins of the Tonga-Kermadec Island arc system, *J. Geophys. Res.*, *75*, 239–254, doi:10.1029/JB075i002p00239.

Koppers, A. A. P., et al. (2012), Limited latitudinal mantle plume motion for the Louisville hotspot, *Nat. Geosci.*, *5*(12), 911–917.

Kroenke, L. W., and P. U. Rodda (1984), *Cenozoic Tectonic Development of the Southwest Pacific*, Tech. Secr. of CCOP/SOPAC c/o Miner. Resour. Dep, edited by Samuel H. Clarke U.S. Geological Survey, Alexandria, Va.

Lonsdale, P. F. (1986), A multibeam reconnaissance of the Tonga trench-axis and its intersection with the Louisville guyot chain, *Mar. Geophys. Res.*, *8*(4), 295–327.

Lutter, W., R. Nowack, and L. Braile (1990), Seismic imaging of upper crustal structure using travel times from the PASSCAL Ouachita experiment, *J. Geophys. Res.*, *95*, 4621–4631, doi:10.1029/JB095iB04p04621.

MacLeod, C. J. (1994), Structure of the outer Tonga forearc at Site 841, in *Proceedings of the Ocean Drilling Program*, *Sci. Results*, vol. 135, pp. 313–329, Texas A&M Univ., College Station.

Malahoff, A., R. H. Feden, and H. S. Fleming (1982), Magnetic anomalies and tectonic fabric of marginal basins north of New Zealand, *J. Geophys. Res.*, *87*, 4109–4125, doi:10.1029/JB087iB05p04109.

Mazengarb, C., and I. G. Speden (2000), *Geology of the Raukumara Area*, 60 pp., Inst. of Geol. and Nucl. Sci. Ltd., Lower Hutt, New Zealand.

Meffre, S., T. J. Falloon, T. J. Crawford, K. Hoernle, F. Hauff, R. A. Duncan, S. H. Bloomer, and D. J. Wright (2012), Basalts erupted along the Tongan fore-arc during subduction initiation: Evidence from geochronology of dredged rocks from the Tonga fore-arc and trench, *Geochem. Geophys. Geosyst.*, *13*, Q12003, doi:10.1029/2012GC004335.

Mortimer, N. (2004), New Zealand's geological foundations, *Gondwana Res.*, *7*, 261–272.

Mortimer, N., R. H. Herzer, P. B. Gans, C. Laporte-Magoni, A. T. Calvert, and D. Bosch (2007), Oligocene–Miocene tectonic evolution of the South Fiji Basin and Northland Plateau, SW Pacific Ocean: Evidence from petrology and dating of dredged rocks, *Mar. Geol.*, *237*, 1–24.

Mortimer, N., P. Gans, J. Palin, S. Meffre, R. Herzer, and D. Skinner (2010), Location and migration of Miocene–Quaternary volcanic arcs in the SW Pacific region, *J. Volcanol. Geotherm. Res.*, *190*(1), 1–10.

Nishizawa, A., N. Takahashi, and S. Abe (1999), Crustal structure and seismicity of the Havre Trough at 26 S, *Geophys. Res. Lett.*, *26*, 2549–2552, doi:10.1029/1999GL900433.

Packham, G., and A. Terrill (1976), Submarine geology of the South Fiji basin, *Initial Rep. Deep Sea Drill. Proj.*, *30*, 617–645.

Peirce, C., and A. B. Watts (2011), R/V Sonne SO215, Cruise Report, The Louisville Ridge - Tonga Trench collision: Implications for subduction zone dynamics, Dep. of Earth Sci., Durham Univ., Durham.

Pelletier, B., and J. Dupont (1990), Erosion, accretion, back-arc extension and slab length along the Kermadec subduction zone, Southwest Pacific, *C. R. Acad. Sci., Ser. II*, *310*(12), 1657–1664.

Pelletier, B., and R. Louat (1989), Seismotectonics and present-day relative plate motions in the Tonga-Lau and Kermadec-Havre region, *Tectonophysics*, *165*(1), 237–250.

Pelletier, B., Y. Lafoy, and F. Missegue (1993), Morphostructure and magnetic fabric of the northwestern North Fiji Basin, *Geophys. Res. Lett.*, *20*, 1151–1154, doi:10.1029/93GL01240.

Rait, G., F. Chanier, and D. W. Waters (1991), Landward- and seaward-directed thrusting accompanying the onset of subduction beneath New Zealand, *Geology*, *19*(3), 230–233.

Ranero, C. R., and R. von Huene (2000), Subduction erosion along the Middle America convergent margin, *Nature*, *404*(6779), 748–752.

Reagan, M. K., W. C. McClelland, G. Girard, K. R. Goff, D. W. Peate, Y. Ohara, and R. J. Stern (2013), The geology of the southern Mariana fore-arc crust: Implications for the scale of Eocene volcanism in the western Pacific, *Earth Planet. Sci. Lett.*, *380*, 41–51.

Reyners, M., D. Eberhart-Phillips, and G. Stuart (1999), A three-dimensional image of shallow subduction: Crustal structure of the Raukumara Peninsula, New Zealand, *Geophys. J. Int.*, *137*, 873–890.

Reyners, M., D. Eberhart-Phillips, and S. Bannister (2011), Tracking repeated subduction of the Hikurangi Plateau beneath New Zealand, *Earth Planet. Sci. Lett.*, *311*(1), 165–171.

Roberts, A. P. (1992), Paleomagnetic constraints on the tectonic rotation of the southern Hikurangi margin, New Zealand, *N. Z. J. Geol. Geophys.*, *35*(3), 311–323.

Rowan, C. J., and A. P. Roberts (2005), Relocation of the tectonic boundary between the Raukumara and Wairoa Domains (East Coast, North Island, New Zealand): Implications for the rotation history of the Hikurangi margin, *N. Z. J. Geol. Geophys.*, *48*(1), 185–196.

Rowan, C. J., and A. P. Roberts (2008), Widespread remagnetizations and a new view of Neogene tectonic rotations within the Australia-Pacific plate boundary zone, New Zealand, *J. Geophys. Res.*, *113*, B03103, doi:10.1029/2006JB004594.

Ruellan, E., J. Delteil, I. Wright, and T. Matsumoto (2003), From rifting to active spreading in the Lau Basin–Havre Trough backarc system (SW Pacific): Locking/unlocking induced by seamount chain subduction, *Geochem. Geophys. Geosyst.*, *4*(5), 8909, doi:10.1029/2001GC000261.

Sandwell, D. T., and W. H. F. Smith (1994), New global marine gravity map/grid based on stacked ERS1, Geosat and Topex altimetry, *Eos Trans. AGU*, *75*(16), 321.

Sandwell, D. T., and W. H. F. Smith (1997), Marine gravity anomaly from Geosat and ERS 1 satellite altimetry, *J. Geophys. Res.*, *102*, 10,039–10,054, doi:10.1029/96JB03223.

Sandwell, D. T., and W. H. F. Smith (2009), Global marine gravity from retracked Geosat and ERS-1 altimetry: Ridge segmentation versus spreading rate, *J. Geophys. Res.*, *114*, B01411, doi:10.1029/2008JB006008.

Sandwell, D. T., D. T. Müller, W. H. F. Smith, E. Garcia, and R. Francis (2014), New global marine gravity from CryoSat-2 and Jacon-1 reveals buried tectonic structure, *Science*, *346*(6205), 65–67.

Schellart, W., G. Lister, and M. Jessell (2002), Analogue modeling of arc and backarc deformation in the New Hebrides arc and North Fiji Basin, *Geology*, *30*(4), 311–314.

Schellart, W. P., G. S. Lister, and V. G. Toy (2006), A Late Cretaceous and Cenozoic reconstruction of the Southwest Pacific region: Tectonics controlled by subduction and slab rollback processes, *Earth Sci. Rev.*, *76*(3-4), 191–233, doi:10.1016/j.earscirev.2006.01.002.

Scherwath, M., et al. (2010), Fore-arc deformation and underplating at the northern Hikurangi margin, New Zealand, *J. Geophys. Res.*, *115*, B06408, doi:10.1029/2009JB00664.

Sdrolias, M., R. Müller, and C. Gaina (2003), Tectonic evolution of the southwest Pacific using constraints from backarc basins, *Geol. Soc. Am. Spec. Pap.*, *372*, 343–359.
Sdrolias, M., R. D. Muller, A. Mauffret, and G. Bernardel (2004), Enigmatic formation of the Norfolk Basin, SW Pacific: A plume influence on back-arc extension, *Geochem. Geophys. Geosyst.*, *5*, Q06005, doi:10.1029/2003GC000643.
Simkin, T., and L. Siebert (2002), *Volcanoes of the World: An Illustrated Catalog of Holocene Volcanoes and Their Eruptions*, *Global Volcanism Program digital Inf. Ser. GVP-3*, E. Venzke, Smithsonian Inst., doi:10.5479/si.GVP.VOTW4-2013.
Smith, W. H. F., and D. T. Sandwell (1997), Global sea floor topography from satellite altimetry and ship depth soundings, *Science*, *277*, 1956–1962.
Stolper, E., and S. Newman (1994), The role of water in the petrogenesis of Mariana trough magmas, *Earth Planet. Sci. Lett.*, *121*(3), 293–325.
Stoneley, R. (1968), A Lower Tertiary decollement on the East Coast, North Island, New Zealand, *N. Z. J. Geol. Geophys.*, *11*, 128–156.
Stratford, W., C. Peirce, M. Funnell, M. Paulatto, A. B. Watts, I. Grevemeyer, and D. Bassett (2015), Effect of Seamount subduction on forearc morphology and seismic structure of the Tonga-Kermadec subduction zone, *Geophys. J. Int.*, *200*, 1503–1522, doi:10.1093/gji/ggu475.
Sutherland, R. (1999), Basement geology and tectonic development of the greater New Zealand region: An interpretation from regional magnetic data, *Tectonophysics*, *308*(3), 341–362.
Sutherland, R., et al. (2009), Reactivation of tectonics, crustal underplating, and uplift after 60 Myr of passive subsidence, Raukumara Basin, Hikurangi-Kermadec fore-arc, New Zealand: Implications for global growth and recycling of continents, *Tectonics*, *28*, TC5017, doi:10.1029/2008TC002356.
Sykes, L. R. (1966), The seismicity and deep structure of island arcs, *J. Geophys. Res.*, *71*, 2981–3006, doi:10.1029/JZ071i012p02981.
Timm, C., D. Bassett, I. J. Graham, M. I. Leybourne, C. de Ronde, J. Woodhead, D. Layton-Matthews, and A. B. Watts (2013), Louisville seamount subduction and its implication on mantle flow beneath the central Tonga-Kermadec arc, *Nat. Commun.*, *4*, 1720.
Timm, C., et al. (2014), Large igneous province subduction: Impact of the Hikurangi Plateau on the Kermadec arc, *Nat. Commun.*, *5*, 4923.
Timm, C., M. Leybourne, R. Wysoczanski, F. Hauff, M. Handler, F. Caratori Tontini, and C. E. J. De Ronde (2016), Trench perpendicular geochemical variation between the two adjacent Kermadec arc volcanoes Rumble II East and West: Role of the subducted Hikurangi Plateau on element recycling in arc magmas, *J. Petrol.*, doi:10.1093/petrology/egw042, in press.
Vannucchi, P., P. Sak, J. P. Morgan, K. Ohkushi, and I. E. S. Scientists (2013), Rapid pulses of uplift, subsidence, and subduction erosion offshore Central America: Implications for building the rock record of convergent margins, *Geology*, *41*(9), 995–998.
Walcott, R. I. (1987), Geodetic strain and the deformational history of the North Island of New Zealand during the late Cainozoic, *Philos. Trans. R. Soc. London*, *321*, 163–181.
Watts, A. B., and M. Talwani (1974), Gravity anomalies seaward of deep-sea trenches and their tectonic implications, *Geophys. J. Int.*, *36*(1), 57–90.
Watts, A. B., and M. Talwani (1975), Gravity effect of downgoing lithospheric slabs beneath island arcs, *Geol. Soc. Am. Bull.*, *86*(1), 1–4.
Watts, A. B., J. Weissel, and R. Larson (1977), Sea-floor spreading in marginal basins of the western Pacific, *Tectonophysics*, *37*(1), 167–181.
Weissel, J., and A. Watts (1975), Tectonic complexities in the South Fiji marginal basin, *Earth Planet. Sci. Lett.*, *28*(2), 121–126.
Wessel, P., and W. H. Smith (1991), Free software helps map and display data, *Eos Trans. AGU*, *72*(41), 441–446, doi:10.1029/90EO00319.
Wessel, P., and W. H. Smith (1995), New version of the Generic Mapping Tools released, *Eos Trans. AGU*, *76*, 329, doi:10.1029/95EO00198.
Wessel, P., and W. H. Smith (1998), New, improved version of Generic Mapping Tools released, *Eos Trans. AGU*, *79*(47), 579, doi:10.1029/98EO00426.
Wright, I. (1994), Nature and tectonic setting of the southern Kermadec submarine arc volcanoes: An overview, *Mar. Geol.*, *118*(3), 217–236.
Wright, I. (1997), Morphology and evolution of the remnant Colville and active Kermadec arc ridges south of 33 30′ S, *Mar. Geophys. Res.*, *19*(2), 177–193.
Wright, I., and J. Gamble (1999), Southern Kermadec submarine caldera arc volcanoes (SW Pacific): Caldera formation by effusive and pyroclastic eruption, *Mar. Geol.*, *161*(2), 207–227.
Wright, I., L. M. Parson, and J. A. Gamble (1996), Evolution and interaction of migrating cross-arc volcanism and backarc rifting; an example from the southern Havre Trough (35 degrees 20′–37 degrees S), *J. Geophys. Res.*, *101*, 22,071–22,086, doi:10.1029/96JB01761.
Wright, I., T. J. Worthington, and J. A. Gamble (2006), New multibeam mapping and geochemistry of the 30 degrees-35 degrees S sector, and overview, of southern Kermadec arc volcanism, *J. Volcanol. Geotherm. Res.*, *149*, 263–296.
Wysoczanski, R., E. Todd, I. Wright, M. Leybourne, J. Hergt, C. Adam, and K. Mackay (2010), Backarc rifting, constructional volcanism and nascent disorganised spreading in the southern Havre Trough backarc rifts (SW Pacific), *J. Volcanol. Geotherm. Res.*, *190*(1), 39–57.
Yan, C., and L. Kroenke (1993), A plate tectonic reconstruction of the southwest Pacific, 0–100 Ma, paper presented at Proceedings of the Ocean Drilling Program, Scientific Results, College Station, Tex.
Zelt, C. A., and R. B. Smith (1992), Seismic traveltime inversion for 2-D crustal velocity structure, *Geophys. J. Int.*, *108*(1), 16–34, doi:10.1111/j.1365-246X.1992.tb00836.x.
Zhong, S., and M. Gurnis (1992), Viscous flow model of a subduction zone with a faulted lithosphere: Long and short wavelength topography, gravity and geoid, *Geophys. Res. Lett.*, *19*, 1891–1894, doi:10.1029/92GL02142.
Zhong, S., and M. Gurnis (1994), Controls on trench topography from dynamic models of subducted slabs, *J. Geophys. Res.*, *99*, 15,683–15,695, doi:10.1029/94JB00809.
Zhong, S., M. Gurnis, and L. Moresi (1998), Role of faults, nonlinear rheology, and viscosity structure in generating plates from instantaneous mantle flow models, *J. Geophys. Res.*, *103*, 15,255–15,268, doi:10.1029/98JB00605.